Defluoridation chemistry of synthetic hydroxyapatite at nano scale: Equilibrium and kinetic studies

C. Sairam Sundaram [a], Natrayasamy Viswanathan [b], S. Meenakshi [b],*

[a] *Department of Science and Humanities, Karaikal, Polytechnic College, Karaikal 609609, Puducherry, India*
[b] *Department of Chemistry, Gandhigram Rural University, Gandhigram 624302, Tamilnadu, India*

Abstract

This study describes the advantages of nano-hydroxyapatite (n-HAp), a cost effective sorbent for fluoride removal. n-HAp possesses a maximum defluoridation capacity [DC] of 1845 mg F^-/kg which is comparable with that of activated alumina, a defluoridation agent commonly used in the aqueous defluoridation technology. A new mechanism of fluoride removal by n-HAp was proposed in which it is established that this material removes fluoride by both ion-exchange and adsorption process. The n-HAp and fluoride-sorbed n-HAp were characterized using XRD, FTIR and TEM studies. The fluoride sorption was reasonably explained with Langmuir, Freundlich and Redlich–Peterson isotherms. Thermodynamic parameters such as $\Delta G°$, $\Delta H°$, $\Delta S°$ and E_a were calculated in order to understand the nature of sorption process. The sorption process was found to be controlled by pseudo-second-order and pore diffusion models. Field studies were carried out with the fluoride containing water sample collected from a nearby fluoride endemic area in order to test the suitability of n-HAp material as a defluoridating agent at field condition.
© 2007 Elsevier B.V. All rights reserved.

Keywords: Defluoridation; n-HAp; Langmuir; Freundlich; Redlich–Peterson; Pseudo-first-order; Pseudo-second-order; Particle and pore diffusion; Adsorption; Ion-exchange

1. Introduction

Fluoride ion in drinking water is known for both beneficial and detrimental effects on health. Consumption of drinking water containing excessive fluoride above 1.5 ppm leads to different forms of fluorosis. Removal of fluoride from water sources is of great scientific and practical interest. Fluoride from drinking water can be removed by either ion-exchange/adsorption process or by coagulation and precipitation process. Based on these processes several defluoridation methods have been proposed. These involve use of alum, lime, aluminium sulphate, magnesite, alumina, activated alumina and synthetic tri-calcium phosphate etc. [1,2]. Recently membrane process such as reverse osmosis [3], electrodialysis [4], nanofiltration [5] and Donnan dialysis [6] were investigated to reduce concentration of fluoride in water.

Nanomaterials offer new possibilities to chemists. All aspects concerning chemistry are modified in the nano scale. The surface properties, electronic structure, coordination etc., get modified when material dimensions reach the nanoscale. Traditional chemistry of the materials may completely become newer and novel chemistry may evolve as a function of size. Nanoparticles could be effectively employed for the removal of toxic chemicals from water as most of the toxic chemicals are removed by adsorption which depends on the surface site. n-HAp is widely used in the process of water treatment. Research works on the removal of cadmium, oxovanadium, cobalt, lead and zinc using hydroxyapatite (HAp) have been reported [7–11]. The authors in a recent paper reported that the adsorption mechanism is the more favorable mechanism for fluoride removal [12]. Hence in the present study, an attempt has been made to study the defluoridation efficiency of synthesized hydroxyapatite (HAp) at nano scale. Though the removal of fluoride using HAp [13,14] has been reported earlier, the authors felt that the use of n-HAp could definitely give a new dimension in the field of defluoridation, hence defluoridation experiments were carried out using the synthesized n-HAp.

HAp is a calcium phosphate based bioceramic and used in the medical field as it is the main component of the hard tissues of living bodies such as bones, teeth, etc. [15]. n-HAp is synthesized

Corresponding author. Tel.: +91 451 2452371; fax: +91 451 2454466.
E-mail address: drs_meena@rediffmail.com (S. Meenakshi).

Defluoridation chemistry of synthetic hydroxyapatite at nano scale: Equilibrium and kinetic studies

C. Sairam Sundaram, Natrayasamy Viswanathan, S. Meenakshi

variety of ceramic processing routes including precipitation, hydrothermal processing routes, etc. [16]. However, precipitation method appears more favourable, since the method of preparation is very simple, cost effective and eco- which in turn make the process easily acceptable by the

In the present study, n-HAp was synthesized in the laboratory by precipitation method and defluoridation studies were carried out under various equilibrating conditions like the effect of contact time, dose, pH and in presence of competi- anions. The equilibrium and kinetic studies of defluoridation of n-HAp were thoroughly discussed which would definitely throw more light in understanding the defluoridation mechanism of n-HAp.

2. Materials and methods

2.1. Synthesis of n-HAp

Synthesis of n-HAp involves the reaction of calcium hydrox- ide and orthophosphoric acid with a Ca/P ratio close to 1.67. pH level of the reaction should be maintained at 7.5 otherwise it may lead to the formation of calcium monophosphate and calcium dehydrates [17]. The synthesis involved the initial for- mation of 0.5 M calcium hydroxide suspension. The suspension was vigorously stirred degassed and heated for 1 h before and during the acid addition. Then 0.3 M orthophosphoric acid was added dropwise at a drip rate of 1–2 drops to form a gelatinous precipitate at 40–42 °C. The pH level was controlled by the addi- tion of NH₄OH solution. The precipitate was left in the mother solution overnight and supernant was decanted. The precipitate was washed with distilled water and then oven dried at 80 °C overnight. Then it was calcined at 400 °C to get a fine n-HAp $Ca_{10}PO_4(OH)_2$ powder.

2.2. Characterisation of n-HAp

The synthesized n-HAp powder was characterized by trans- mission electron microscope (TEM), X-ray diffraction (XRD) and fourier transform infrared spectrometer (FTIR). The size and shape of n-HAp was measured by TEM (CM 200-PANalytical make). XRD spectra of synthesized n-HAp were identified by X'per PRO model-PANalytical make. XRD was used to deter- mine the crystalline phases present in n-HAp. FTIR spectra of the samples as solid by diluting in KBr pellets were recorded with JASCO-460 plus model. The results of FTIR spectrome- ter were used to confirm the functional groups present and also fluoride sorption on the n-HAp.

2.3. Adsorption experiments

The sorption isotherm and kinetic experiments were per- formed by batch equilibration method. Stock solution of sodium fluoride containing 100 mg/L was prepared and this was used for fluoride sorption experiments. The batch adsorption experi- ments were carried out by mixing 0.25 g of n-HAp with 50 mL of 10 mg/L as initial fluoride concentration. The contents were

shaken thoroughly using a thermostated shaker rotating at a speed of 200 rpm. The solution was then filtered and the resid- ual fluoride ion concentration was measured using expandable ion analyser EA 940 and the fluoride ion selective electrode BN 9609 (USA make). The pH measurements were carried out with the same instrument with pH electrode. The kinetic and thermodynamic parameters of the adsorption were estab- lished by conducting the experiments at 303, 313 and 323 K in a temperature controlled mechanical shaker. The defluoridation capacity [DC] of the sorbents were studied at different condi- tions like various mass of sorbents, contact time of the sorbent for maximum defluoridation, pH of the medium and the effect of co-anions on defluoridation. The concentrations of NO_3^- and SO_4^{2-} ions were determined using UV–vis spectrophotometer (PerkinElmer–Lambda 35) [18]. All other water quality param- eters were analysed by using standard methods [18]. The pH at zero point charge (pH$_{zpc}$) of n-HAp was measured using the pH drift method [19].

Computations were made using Microcal Origin (Version 6.0) software. The goodness of fit was discussed using regres- sion correlation coefficient (r) and coefficient of determination (r^2).

3. Results and discussion

3.1. Characterisation of the sorbent

In order to characterize n-HAp, XRD, FTIR and TEM anal- ysis were carried out on synthesized n-HAp and fluoride treated samples. The XRD pattern of synthesized n-HAp and the sample treated with fluoride was presented in Fig. 1a and b, respectively.
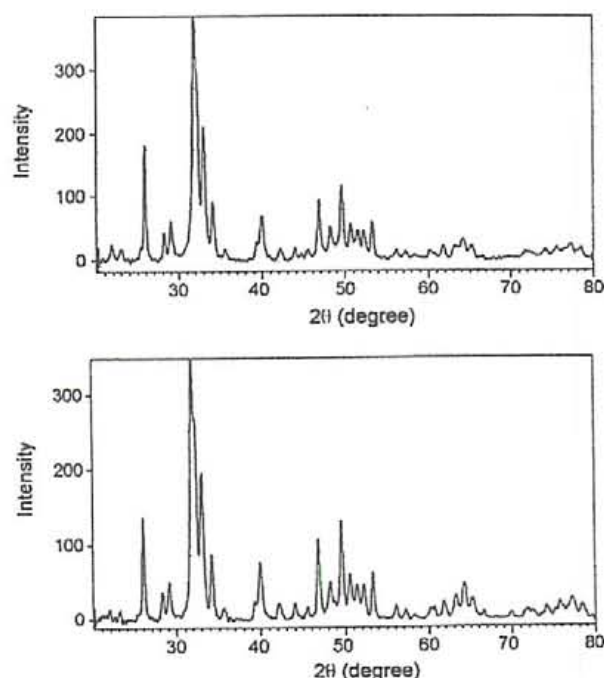

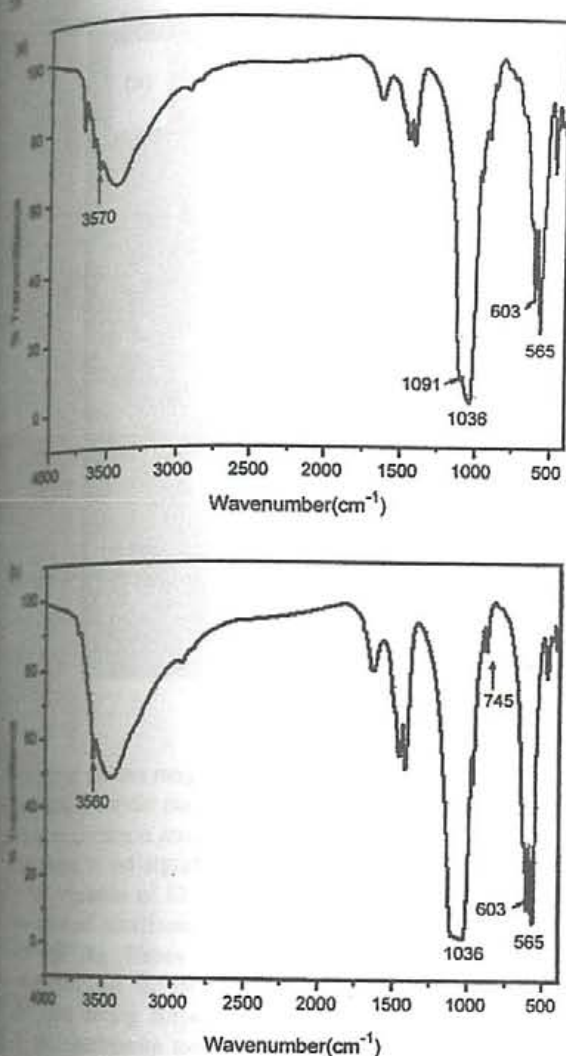Fig. 1. XRD patterns of (a) n-HAp and (b) fluoride sorbed n-HAp.

Fig. 2. FTIR spectra of (a) n-HAp and (b) fluoride treated n-HAp.

crystalline peaks at $2\theta = 25.9°$, $32°$, $33°$, $35.5°$ and $40°$ confirm the formation of hydroxyapatite structure [20]. There is no change in the XRD pattern of n-HAp after treatment with fluoride. Similar results are reported by Diaz-Nava et al. while studying the fluoride sorption on zeolites.

Fig. 2a and b represents FTIR spectra of the samples before and after treatment with fluoride. The bands at $3570\,cm^{-1}$ belong to the stretching vibrations of hydroxyl. The bands of 1040, 603 and 566 cm^{-1} belong to the phosphate stretching and bending vibrations, respectively [22]. There is a reduction in the intensity of OH bands at 3570 and $630\,cm^{-1}$ with some displacement to lower frequencies in fluoride treated n-HAp which may be due to fluoride adsorption/exchange. The apparition of new band at 745 cm^{-1} in fluoride treated n-HAp confirms the formation of OH-F bond.

SEM micrographs of n-HAp powder were presented in Fig. 3a-c respectively. The size of the powder is about 200 nm with cylindrical rod like shape. The particles are of homogeneous microstructure and formed a uniform nanomaterial.

3.2. Effect of contact time and dose

The sorption of fluoride ion on n-HAp has been investigated as a function of contact time in the range of 10–60 min with 10 mg/L as initial fluoride concentration at room temperature. The effect of defluoriation capacity (DC) with contact time is shown in Fig. 4. It is evident that almost saturation was reached after 30 min. Hence 30 min was fixed as the period of contact for further studies. If the sorption process is only controlled by ion exchange mechanism, the saturation of the material would have been reached very soon. But n-HAp reached saturation only after 30 min suggesting that the process is also governed by adsorption which is rather slow than the ion-exchange process [12,23]. In order to fix the optimum dosage defluoridation experiments were carried out with various dosages of n-HAp ranging from 0.1 to 1.0 g with 10 mg/L as initial fluoride concentration and the results were given in Fig. 5. As it is obvious, the percent fluoride removal increases with increase in the dose of the sorbent due to more active sites with an increase in amount of sorbent [24]. The optimum dosage was fixed as 0.25 g for further studies as this dosage found to bring down the level of fluoride within the tolerance limit.

3.3. Effect of pH

The pH of the aqueous solution plays an important role which controls the adsorption at the water adsorbent interface [25]. Therefore the adsorption of fluoride on the n-HAp was examined at various pH ranges ranging from 3 to 11 with 10 mg/L as initial fluoride concentration at room temperature and was presented in Fig. 6. The pH of the working solution is controlled by adding sufficient HCl/NaOH solution. It can be inferred that fluoride removal decreases with increasing pH where the maximum DC is recorded as $1845\,mgF^-/kg$ at pH 3 and only $570\,mgF^-/kg$ was removed at pH 11. Similar observations are observed by Karthikeyan et al. [26] when activated alumina was used as sorbent. This can be explained due to the change in surface charge of the adsorbent. It is well established that the surface is highly protonated in acidic medium and therefore maximum fluoride removal in acidic medium is attributed to the gradual increase in attractive forces between positively charged surface and negatively charged fluoride ions. Lower DC in alkaline medium can be explained by the fact that the surface acquires negative charge in alkaline pH and hence there is a repulsion between the negatively charged surface and fluoride. This argument is very well supported by zero point charge studies (cf. Fig. 7). The pH_{zpc} value of n-HAp was found to be 7.88. Chemisorption occurs below the pH_{zpc} value and above pH_{zpc} value it will be physisorption in addition to ion exchange. This mechanism of fluoride removal is explained in Schemes 1–3.

3.4. Effect of other anions

The DC of n-HAp in presence of competing anions like sulphate, chloride, nitrate and bicarbonate which are usually present in water was experimentally verified with the concen-
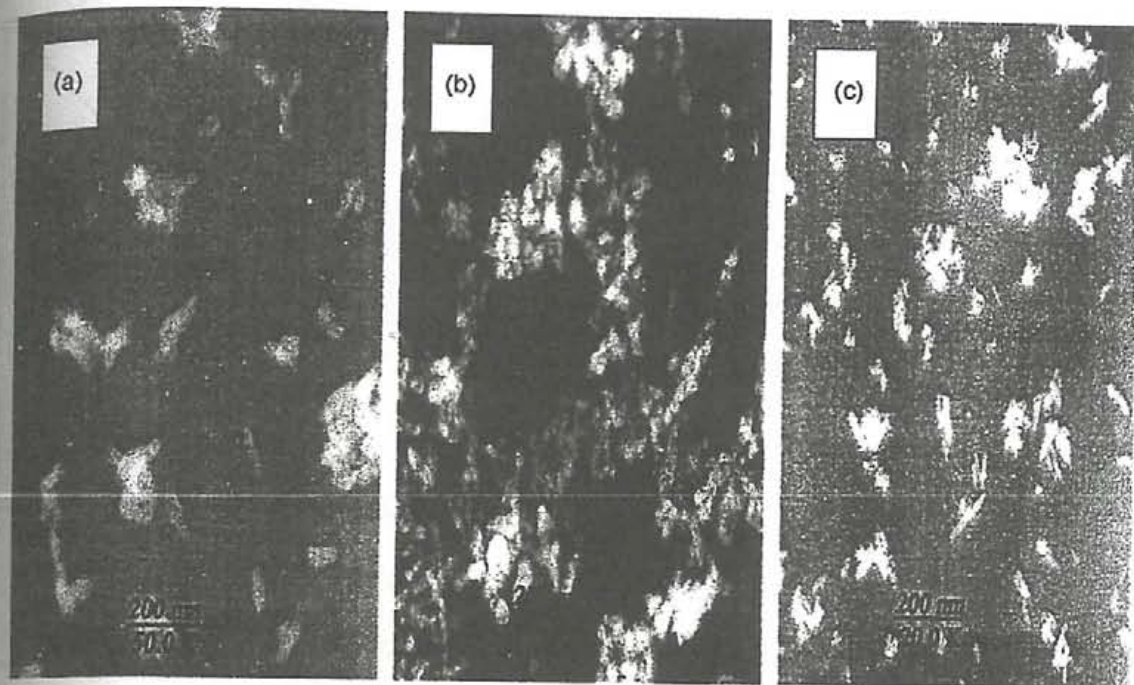
Fig. 3. (a–c) TEM images of n-HAp.

tions of anions ranging from 100 to 500 mg/L with 10 mg/L initial fluoride concentration at 303 K. Fig. 8 shows the effect of common anions on DC of n-HAp. It can be inferred that there is no significant influence on DC of the material in the presence of Cl^-, SO_4^{2-} and NO_3^- ions. However, in presence of bicarbonate ion the DC decreased from 1290 to 856 mgF$^-$/kg. Hence from the above discussions it can be concluded that the bicarbonate ions will compete with fluoride ions during sorption. A similar interfering role on DC by the bicarbonate ion was reported in the case of defluoridation property of activated alumina and montmorillonite clay [26,27].

3.5. Adsorption isotherms

The sorption isotherms express the specific relation between the concentration of sorbate and its degree of accumulation onto sorbent surface at constant temperature. The fluoride sorption capacity of n-HAp has been evaluated using three different isotherms namely Langmuir, Freundlich and Redlich–Peterson isotherms.

The linear form of Freundlich isotherm [28] is represented in Table 1. q_e is the amount of fluoride adsorbed per unit weight of the sorbent at equilibrium (mg/g), C_e is the equilibrium concentration of fluoride in solution (mg/L), k_F is a measure of

Fig. 4. Effect of contact time on the DC of n-HAp.

Fig. 5. Effect of sorbent dose in the percent fluoride removal of n-HAp.

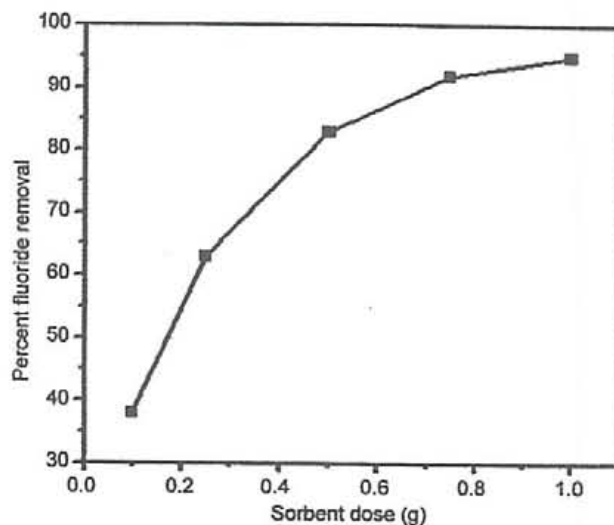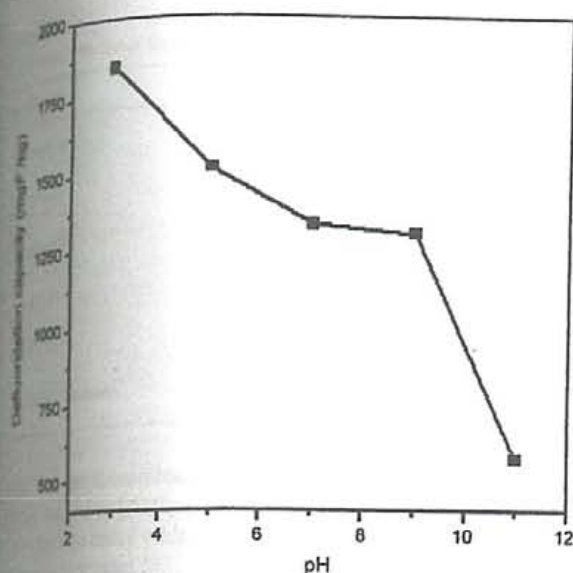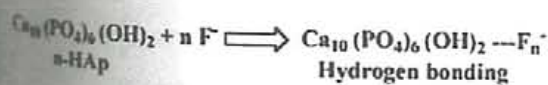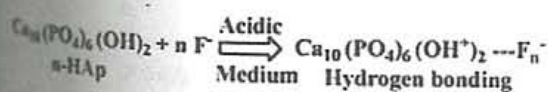Fig. 6. Effect of pH.
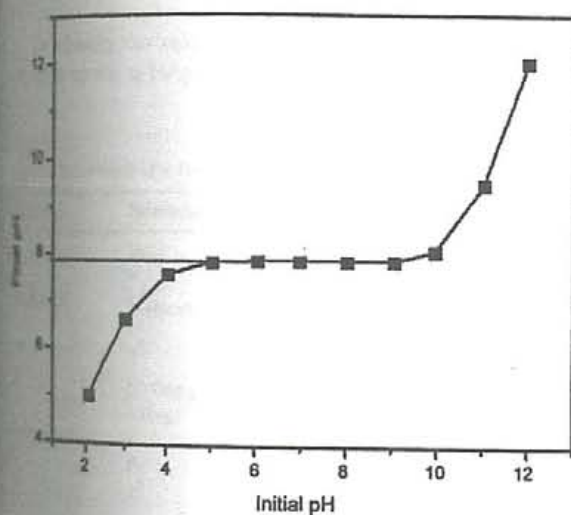
Fig. 7. Determination of pH$_{zpc}$ of n-HAp.

$$Ca_{10}(PO_4)_6(OH)_2 + n\ F^- \Longrightarrow Ca_{10}(PO_4)_6(OH)_2 \text{---} F_n^-$$
n-HAp   Hydrogen bonding

Scheme 1. Fluoride removal of n-HAp by adsorption mechanism.

$$Ca_{10}(PO_4)_6(OH)_2 + n\ F^- \xrightarrow[\text{Medium}]{\text{Acidic}} Ca_{10}(PO_4)_6(OH^+)_2 \text{---} F_n^-$$
n-HAp   Hydrogen bonding

Scheme 2. Mechanism of fluoride removal in acidic medium.

$$Ca_{10}(PO_4)_6(OH)_2 + 2\ F^- \Longrightarrow Ca_{10}(PO_4)_6 F_2 + 2\ OH^-$$
n-HAp   Fluoroapatite
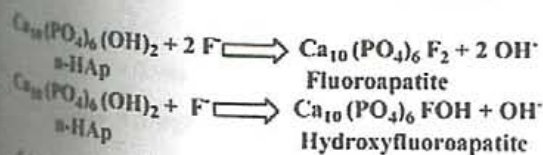
$$Ca_{10}(PO_4)_6(OH)_2 + F^- \Longrightarrow Ca_{10}(PO_4)_6 FOH + OH^-$$
n-HAp   Hydroxyfluoroapatite

Scheme 3. Fluoride removal of n-HAp by ion-exchange mechanism.

Fig. 8. Effect of competitor anions in the DC of n-HAp.

adsorption capacity and $1/n$ is the adsorption intensity. The Freundlich isotherm constants k_F and n were calculated from the slope and intercept of the plot of $\log q_e$ versus $\log C_e$ and were presented in Table 2. The values of $1/n$ are lying between 0.1 and 1.0 and the n value lying in the range of 1–10 confirms the favourable conditions for adsorption [12].

Langmuir isotherm [29] model has four types and are listed in Table 1. The sorption capacity ($Q°$) is the amount of adsorbate at complete monolayer coverage (mg/g), it gives the maximum sorption capacity of sorbent and b (L/mg) is the Langmuir isotherm constant that relates to the energy of adsorption. The respective values of $Q°$ and b were determined from the slope and intercept of the straight line plot of C_e/q_e versus C_e and are presented in Table 2. From Table 2 it is clear that the higher r values for the sorption of fluoride on n-HAp were shown by Type I and Type II Langmuir isotherms.
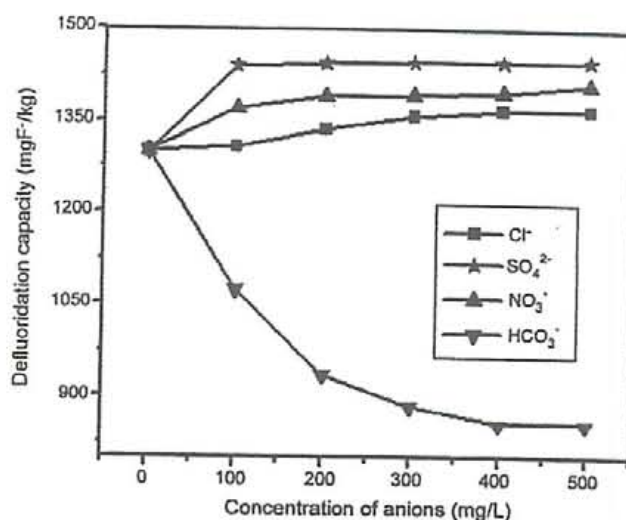
In order to find out the feasibility of the isotherm, the essential characteristics of the Langmuir isotherm can be expressed in terms of a dimensionless constant separation factor or equilibrium parameter, R_L [30],

$$R_L = \frac{1}{1 + bC_0}, \tag{1}$$

where b is the Langmuir isotherm constant and C_0 is the initial concentration of fluoride (mg/L). The R_L (Eq. [1]) values lying between 0 and 1 calculated from Langmuir models are shown in Table 2 indicates the favorable conditions for adsorption.

Redlich–Peterson isotherm [31] is a three parameter isotherm which incorporates the features of both Langmuir and Freundlich isotherms and its linear form is shown in Table 1. The isotherm constants A, B and g can be evaluated from the linear form of the Redlich–Peterson equation using a trial-and-error optimization method and were presented in Table 2. A general trial-and-error procedure which is applicable to computer operation was developed to determine the regression coefficient (r) for a series of values of A for the linear regression of $\ln C_e$ on $\ln [A(C_e/q_e) - 1]$ and to obtain the best value of A which yields a maximum optimized value of r and the respective values of g

Table 1
...... with linear forms and their plots

		Linear form	Plot
Freundlich	$q_e = k_F C_e^{1/n}$	$\log q_e = \log k_F + \dfrac{1}{n} \log C_e$	$\log q_e$ vs. $\log C_e$
Langmuir-1	$q_e = \dfrac{Q^\circ b C_e}{1 + b C_e}$	$\dfrac{C_e}{q_e} = \dfrac{1}{Q^\circ b} + \dfrac{C_e}{Q^\circ}$	$\dfrac{C_e}{q_e}$ vs. C_e
Langmuir-2		$\dfrac{1}{q_e} = \left[\dfrac{1}{Q^\circ b}\right] \dfrac{1}{C_e} + \dfrac{1}{Q^\circ}$	$\dfrac{1}{q_e}$ vs. $\dfrac{1}{C_e}$
Langmuir-3		$q_e = Q^\circ - \left[\dfrac{1}{b}\right] \dfrac{q_e}{C_e}$	q_e vs. $\dfrac{q_e}{C_e}$
Langmuir-4		$\dfrac{q_e}{C_e} = bQ^\circ - bq_e$	$\dfrac{q_e}{C_e}$ vs. q_e
Redlich-Peterson	$q_e = \dfrac{AC_e}{1 + BC_e^g}$	$\ln\left(A\dfrac{C_e}{q_e} - 1\right) = g \ln C_e + \ln B$	$\ln\left(A\dfrac{C_e}{q_e} - 1\right)$ vs. $\ln C_e$

... B were determined from the slope and intercept of the plot ... C_e versus $\ln[A(C_e/q_e)-1]$. It can be seen that the values of g .... close to unity which suggests the isotherms are approaching Langmuir model [32].

3.6. Chi-square analysis

To identify the suitable isotherm model for the sorption of fluoride on the n-HAp, this analysis has been carried out. The

Table 2
Isotherm parameters of n-HAp obtained at different temperatures

Isotherm	Parameters	303 K	313 K	323 K
Freundlich	$1/n$	0.318	0.215	0.285
	n	3.14	4.65	3.51
	k_F (mg/g)(L/mg)$^{1/n}$	0.554	0.706	0.687
	r	0.897	0.867	0.991
	χ^2	2.78E–3	2.18E–3	2.22E–4
Langmuir-1	Q° (mg/g)	1.288	1.204	1.457
	b (L/g)	0.533	1.026	0.612
	r	0.984	0.994	1.00
	R_L	0.211	0.122	0.189
	χ^2	1.94E–3	1.55E–3	1.12E–5
Langmuir-2	Q° (mg/g)	3.113	1.727	1.676
	b (L/g)	0.657	0.731	0.682
	r	0.945	0.926	1.00
	R_L	0.178	0.163	0.173
	χ^2	0.878	0.087	0.030
Langmuir-3	Q° (mg/g)	0.494	0.807	0.879
	b (L/g)	3.058	1.684	1.665
	r	0.835	0.846	0.999
	R_L	0.044	0.078	0.079
	χ^2	0.500	0.113	0.113
Langmuir-4	Q° (mg/g)	0.626	1.039	0.881
	b (L/g)	2.134	1.206	1.662
	r	0.835	0.846	0.999
	R_L	0.063	0.106	0.079
	χ^2	0.246	0.017	0.112
Redlich-Peterson	A (L/mg)	1.00	1.53	15.60
	g	0.90	1.12	1.15
	B (L/mg)^g	1.31	1.08	2.43
	r	0.932	0.986	0.841
	χ^2	0.489	0.668	0.507

chi-square statistic test is basically the sum of the squares of the differences between the experimental data and data obtained by calculating from models, with each squared difference divided by the corresponding data obtained by calculating from the models. The equivalent mathematical statement is:

$$\chi^2 = \sum \frac{(q_e - q_{e,m})^2}{q_{e,m}}, \qquad (2)$$

where $q_{e,m}$ is equilibrium capacity obtained by calculating from the model (mg/g) and q_e is experimental data of the equilibrium capacity (mg/g). If the data from the model are similar to the experimental data, χ^2 will be a small number, while if they differ; χ^2 will be a bigger number. Therefore, it is necessary to also analyse the data set using the non-linear chi-square test to confirm the best-fit isotherm for the sorption system [12].

The corresponding chi-square values (Eq. (2)) for all the isotherms were presented in Table 2. From the chi-square values the best fit for the sorption of fluoride on n-HAp is in the following order:

Langmuir–1 > Freundlich > Langmuir–4 > Langmuir–3 > Langmuir–2 > Redlich–Peterson

$\overrightarrow{\qquad\qquad}$
χ^2 values increases

The isotherm values fits well for both Langmuir-1 and Freundlich isotherms, but better fits to Langmuir-1 isotherm model indicating monolayer chemisorption being dominant.

3.7. Thermodynamic investigations 热力学的研究

Thermodynamic parameters associated with the adsorption viz., standard free energy change (ΔG°), standard enthalpy change (ΔH°), standard entropy change (ΔS°) and activation energy (E_a) were calculated as follows.

The free energy of sorption process, considering the sorption distribution coefficient K_o, is given by the equation:

$$\Delta G^\circ = -RT \ln K_o, \qquad (3)$$

where ΔG° is the standard free energy change (kJ/mol), T is the temperature in Kelvin and R is the universal gas constant (8.314 J mol^{-1} K^{-1}). The sorption distribution coefficient K_o for the sorption reaction was determined from the slope of the plot $\ln(q_e/C_e)$ against C_e at different temperatures and extrapolating

according to the method suggested by Khan and Singh

The sorption distribution coefficient may be expressed in terms of $\Delta H°$ and $\Delta S°$ as a function of temperature:

$$\ln k_0 = \frac{\Delta H°}{RT} + \frac{\Delta S°}{R},$$
(4)

where $\Delta H°$ is the standard enthalpy change (kJ/mol) and $\Delta S°$ standard entropy change (kJ/mol K). The values of $\Delta H°$ and $\Delta S°$ can be obtained from the slope and intercept of a plot of $\ln k_0$ against $1/T$.

A modified Arrhenius-type equation related to the surface coverage (θ) is sticking probability, S^*. This is a function of the adsorbate/adsorbent system, which is a measure of the potential of the adsorbate to remain on the adsorbent indefinitely [34] and can be expressed as:

$$S^* = (1 - \theta) \exp - \left(\frac{E_a}{RT}\right),$$
(5)

where θ is surface coverage,

$$\theta = \left(1 - \frac{C_e}{C_0}\right),$$
(6)

where C_0 and C_e are the initial and equilibrium fluoride ion concentrations respectively. The plot of $\ln(1 - \theta)$ against $1/T$ will give a linear plot with intercept of $\ln S^*$ and slope of E_a/R. The effect of temperature a major influencing factor in the sorption process, the sorption of n-HAp was monitored at three different temperatures 303, 313 and 323 K under the optimized conditions and thermodynamic parameters viz., $\Delta G°$, $\Delta H°$, $\Delta S°$ and S^* were calculated from Eqs. (3)–(6) and presented in Table 3. It may be deduced from negative values of $\Delta G°$ indicates the sorption process is spontaneous. The positive value of $\Delta H°$ and indicates the endothermic nature of the sorption process. The positive value $\Delta S°$ shows the increasing randomness during the sorption of fluoride ions onto n-HAp. The value of S^* is found 0.1 which is very close to zero indicates that the adsorption follows chemisorption [34].

3.8. Sorption dynamics

To understand the sorption mechanism such as mass transfer and chemical reaction processes, two types of models viz., reaction-based and diffusion-based models were applied to test

Table 3

Thermodynamic parameters obtained at different temperatures during fluoride sorption on n-HAp

Thermodynamic parameters		n-HAp
$\Delta G°$ (kJ mol^{-1})	303 K	−5.08
	313 K	−4.73
	323 K	−4.92
$\Delta H°$ (kJ mol^{-1})		7.63
$\Delta S°$ (kJ mol^{-1} K^{-1})		8.71
E_a (kJ mol^{-1})		4.58
S^*		0.10

Table 4

Lagergren constants for sorption of fluoride on n-HAp at different temperatures

C_0 (mg/L)	Mass (g)	303 K		313 K		323 K	
		k_{ad} (min^{-1})	r	k_{ad} (min^{-1})	r	k_{ad} (min^{-1})	r
7	0.25	0.128	0.840	0.137	0.958	0.157	0.983
9	0.25	0.148	0.954	0.127	0.903	0.133	0.892
11	0.25	0.154	0.974	0.145	0.951	0.132	0.860
13	0.25	0.148	0.964	0.199	0.969	0.163	0.850

the fitness of experimental data [35]. The prediction of the batch sorption kinetics is necessary for the design of industrial adsorption column.

3.8.1. Reaction-based models

In order to investigate the sorption mechanism of fluoride removal, pseudo-first-order and pseudo-second-order kinetic models have been used at different experimental conditions.

A simple pseudo-first-order kinetic model [36] is represented as:

$$\log(q_e - q_t) = \log q_e - \frac{k_{ad}}{2.303}t,$$
(7)

where q_t is the amount of fluoride on the surface of the sorbent n-HAp at time t (mg/g) and k_{ad} is the equilibrium rate constant of pseudo-first-order sorption (min^{-1}). The straight-line plots of $\log(q_e - q_t)$ against t for different experimental conditions will give the value of the rate constants (k_{ad}). Linear plots of $\log(q_e - q_t)$ against t give straight line which indicates the applicability of Lagergren equation. The values of k_{ad} and the correlation coefficient (r) computed from these plots were given in Table 4. The pseudo-first-order model seems to be viable because of the higher correlation coefficient (r).

In addition, the pseudo-second-order model is also widely used. Though there are four types of linear pseudo-second-order kinetic models [37] the most popular linear form used has the equation:

$$\frac{t}{q_t} = \frac{1}{h} + \frac{t}{q_e},$$
(8)

where $q_t = q_e^2 kt/(1 + q_e kt)$, amount of fluoride on the surface of the n-HAp at any time, t (mg/g), k is the pseudo-second-order rate constant (g/mg min), q_e is the amount fluoride ion sorbed at equilibrium (mg/g) and the initial sorption rate, $h = kq_e^2$ (mg/g min). The value of q_e (1/slope), k (slope^2/intercept) and h (1/intercept) of the pseudo-second-order equation can be found out experimentally by plotting t/q_t against t.

The fitness of the pseudo-second-order model (Eq. (8)) on the fluoride sorption on n-HAp was also analysed. The plot of t versus t/q_t gives a straight line with higher correlation coefficient r values, which is higher than that observed with pseudo-first-order model indicating the applicability of the pseudo-second-order model and the values are shown in Table 5. The values of q_e increased with increase in initial concentration and it also increased with increase in temperature. The values of rate constant (k) have also increased with temperature indicating chemisorption.

in a linear analysis, different linear forms of the same model would significantly affect calculations of the parameters [38]. According to Ho [37], a non-linear method could be a better way to obtain the kinetic parameters and would be able to avoid such errors. For the non-linear method, a trial and error procedure which is applicable to computer operation was developed to determine the pseudo-second-order rate parameters by optimization routine to maximize the coefficient of determination (r) between experimental data and pseudo-second-order model using the solver add-in with Microsoft's spreadsheet, Microsoft Excel.

In this study, the coefficient of determination, r^2 was calculated using Eq. (9) to test the best-fit of the linear and non-linear pseudo-second-order kinetic model to the experimental data:

$$r = \sum \frac{(q_m - \bar{q}_t)^2}{(q_m - \bar{q}_t)^2 + (q_m - q_t)^2}, \tag{9}$$

where q_m is the amount of fluoride ion on the surface of the n-HAp at any time, t (mg/g) obtained from the second-order kinetic model, q_t is the amount of fluoride ion on the surface of the n-HAp at any time, t (mg/g) obtained from experiment and $\bar{q}_t$ is the average of q_t (mg/g). The coefficient of determination r^2 calculated from both linear and non-linear methods were presented in Table 5 with the experimental data for q_e, k and h. Higher values of r^2 in non-linear method indicates the better applicability of non-linear pseudo-second-order method than the linear one.

3.8.2. Diffusion-based models

For a solid–liquid sorption process, the solute transfer is usually characterised either by particle diffusion or pore diffusion control.

A simple equation for the particle diffusion controlled sorption process [12,39] is as follows:

$$\ln\left(1 - \frac{C_t}{C_e}\right) = -k_p t, \tag{10}$$

where k_p is the particle rate constant (min^{-1}). The value of particle rate constant is obtained by the slope of $\ln(1 - C_t/C_e)$ against t.

The pore diffusion model used here refers to the theory proposed by Weber and Morris [40,41]. The intraparticle diffusion equation is given below:

$$q_t = k_i t^{1/2}, \tag{11}$$

where k_i is the intraparticle rate constant (mg/g min$^{0.5}$). The slope of the plot of q_t against $t^{1/2}$ will give the value of intraparticle rate constant. On plotting q_t versus $t^{0.5}$ gives an initial curve followed by a straight line which indicates that two types of mechanisms are involved in the adsorption process. The initial curve represents the boundary layer effect while the linear part corresponds to intraparticle diffusion.

Both particle (Eq. (10)) and pore (Eq. (11)) diffusion models have been applied and the values of k_p and k_i were presented in Table 6. Higher r values in both the cases indicate the possibility of sorption process being controlled by both the particle and pore diffusion models.

3.9. Fitness of the sorption kinetic models

The assessment of the employed kinetic models for fitting the sorption data was made by calculating the squared sum of errors [SSE]. Lower values of SSE show better fit to sorption data and can give an indication of the sorption mechanism [12].

$$SSE = \sum \frac{(q_{t,e} - q_{t,m})^2}{q_{t,e}^2}, \tag{12}$$

where $q_{t,e}$ and $q_{t,m}$ are the experimental sorption capacity of fluoride (mg/g) at time t and the corresponding value which is obtained from the kinetic models. SSE values (Eq. (12)) of the reaction-based and diffusion-based kinetic models were computed and summarized in Table 7. It is assumed that the model which gives the lowest SSE values is the best model for this system and then the mechanism of sorption can be explained based on that model. It was observed from Table 7 that pseudo-second-order model and pore diffusion model seems to be better fit than the other two models (pseudo-first-order and particle diffusion models) for representing the kinetics of fluoride sorption on n-HAp.

3.10. Mechanism of fluoride sorption on n-HAp

The fluoride removal by n-HAp appears to be controlled by both adsorption and ion-exchange mechanisms. In fluoride solu-

Table 5

Comparison of the linear and non-linear methods of pseudo-second-order kinetic parameters of n-HAp based on coefficient of determination (r^2)

Methods	Parameters	303 K				313 K				323 K			
		7 mg/L	9 mg/L	11 mg/L	13 mg/L	7 mg/L	9 mg/L	11 mg/L	13 mg/L	7 mg/L	9 mg/L	11 mg/L	13 mg/L
Linear	q_e (mg/g)	0.804	0.961	1.098	1.068	0.881	1.034	1.101	1.115	0.915	1.046	1.162	1.252
	k (g/mg min)	0.412	0.670	0.452	0.479	0.613	0.652	0.735	0.460	1.034	1.125	0.441	0.315
	h (mg/g min)	0.266	0.618	0.545	0.546	0.475	0.698	0.891	0.572	0.865	1.230	0.596	0.494
	r	0.996	0.999	0.999	1.00	1.00	0.999	1.00	0.999	1.00	1.00	0.998	0.998
	r^2	0.838	0.783	0.745	0.761	0.782	0.848	0.799	0.724	0.774	0.872	0.846	0.786
Non-linear	q_e (mg/g)	0.729	0.891	0.989	0.961	0.802	0.983	1.046	0.975	0.869	1.009	1.087	1.127
	k (g/mg min)	0.406	0.664	0.445	0.473	0.959	0.649	0.731	0.452	1.030	1.123	0.438	0.311
	h (mg/g min)	0.216	0.527	0.435	0.436	0.617	0.627	0.800	0.430	0.777	1.144	0.517	0.394
	r^2	0.861	0.831	0.805	0.775	0.794	0.911	0.908	0.697	0.883	0.859	0.891	0.833

...and pore diffusion model parameters for fluoride sorption at different initial concentrations with different temperatures

Mass (g)	303 K				313 K				323 K			
	Particle DM[a]		Pore DM[a]		Particle DM[a]		Pore DM[a]		Particle DM[a]		Pore DM[a]	
	k_p (min^{-1})	r	k_i (mg/g min$^{0.5}$)	r	k_p (min^{-1})	r	k_i (mg/g min$^{0.5}$)	r	k_p (min^{-1})	r	k_i (mg/g min$^{0.5}$)	r
0.25	0.012	0.979	0.058	0.981	0.012	0.984	0.049	0.995	0.010	0.932	0.036	0.958
0.25	0.009	0.956	0.048	0.972	0.010	0.989	0.043	0.993	0.007	0.970	0.030	0.984
0.25	0.001	0.961	0.064	0.972	0.008	0.941	0.046	0.961	0.010	0.985	0.057	0.974
0.25	0.007	0.975	0.063	0.991	0.008	0.959	0.066	0.978	0.011	0.975	0.085	0.985

[a] ...diffusion model.

...sum of errors (SSE) values of kinetic models employed for fluoride sorption on n-HAp

...models	303 K				313 K				323 K			
	7 mg/L	9 mg/L	11 mg/L	13 mg/L	7 mg/L	9 mg/L	11 mg/L	13 mg/L	7 mg/L	9 mg/L	11 mg/L	13 mg/L
...-first-order	2.7E−3	7.9E−3	4.8E−3	5.8E−3	8.9E−3	1.5E−3	1.1E−3	7.5E−5	9.4E−3	1.8E−2	8.5E−3	6.9E−4
...-second-order	2.7E−3	1.8E−3	3.6E−3	3.0E−3	2.9E−3	1.1E−3	1.3E−3	5.3E−3	1.2E−3	3.3E−3	1.8E−3	4.7E−3
...diffusion	0.707	0.750	0.968	0.795	0.697	0.732	0.770	0.769	0.730	0.797	0.733	0.710
...diffusion	0.416	0.600	0.532	0.528	0.554	0.662	0.665	0.527	0.686	0.769	0.599	0.455

...the F$^-$ ions gets adsorbed onto the n-HAp surface as shown ...Scheme 1.

...acidic medium, where the concentration of H$^+$ ion is high ...therefore n-HAp surface acquires positive charge which in ...attracts more fluoride ions and hence there is a significant ...in DC at lower pH. This is illustrated in Scheme 2.

...nature of attractive force between n-HAp and fluoride ...as described above is confirmed by the FTIR results in ...there is an emergence of new peak at 745 cm^{-1}, which ...characteristic of O–H$\cdots$F vibration band in the fluoride ...n-HAp. As the pH increases surface slowly acquire neg- ...charges which would repel fluoride ions and hence the ...removal by electrostatic attraction is ruled out in alkaline ...

...addition, ion exchange mechanism is also involved in flu- ...removal by n-HAp. The OH group present in the n-HAp ...considered as the charge carrier and can get exchanged with ...ions [42]. The mechanism of fluoride removal of n-HAp by ...exchange is represented in Scheme 3.

...it can be concluded that the fluoride removal by n-HAp ...governed by both adsorption and ion-exchange mechanism ...that it can act as an effective defluoridating agent.

...results of n-HAp

...quality parameters	Treatment	
	Before	After
	2.33	0.47
	9.10	8.78
	0.62	0.63
	57.00	53.00
	70.00	0.00
	465.00	453.00
	42.00	39.30
	8.80	7.90

3.11. Field trial

The applicability of the n-HAp in the field condition was also tested with the sample taken from a nearby fluoride-endemic area. The results were presented in Table 8. The concentration of fluoride in the treated water is well within the tolerance limit and there is no significant change in other water quality parameters after treatment.

4. Conclusions

From the above discussions following conclusions were made, fluoride sorption on n-HAp is spontaneous and endothermic. The DC of n-HAp is significantly influenced by pH of the medium. There is no significant influence of other co-anions like chloride, nitrate and sulphate on the DC of n-HAp except bicarbonate ions. The mechanism of fluoride removal of n-HAp follows both adsorption and ion-exchange mechanism. The adsorption pattern follows both Langmuir and Freundlich isotherms, but better fits to Langmuir isotherm particularly Langmuir-1 model. The rate of reaction follows pseudo-second-order kinetics. A non-linear pseudo-second-order model would be a better way to obtain kinetic parameters. The sorption of fluoride ion on n-HAp occurs through intraparticle diffusion pattern. Field trials indicated that n-HAp can be effectively used as an efficient and cost effective defluoridating agent.

References

[1] P. Phantumvanit, Y. Songpaisan, I.J. Moller, A defluoridator for individual households, World Health Forum 9 (1988) 555–558.

[2] N.V. Rao, R. Mohan, C.S. Bhaskaran, Studies on defluoridation of water, J. Fluorine Chem. 41 (1998) 17–24.

[3] S.V. Joshi, S.H. Mehta, A.P. Rao, A.V. Rao, Estimation of sodium fluoride using HPLC in reverse osmosis experiments, Water Treat. 10 (1992) 307–312.

S.K. Adihikary, U.K. Tipnis, W.P. Harkare, K.P. Govindan, Defluoridation during desalination of brackish water by electrodialysis, Desalination 71 (1989) 301–312.

R. Simons, Trace element removal from ash dam waters by nanofiltration and diffusion dialysis, Desalination 89 (1993) 325–341.

A. Dieye, Defluoridation des eaux par dialyse ionique croisee, Thesis, University Paris XII, 1995.

G. Lusvardi, G. Malavasi, L. Menabue, M. Saladini, Removal of cadmium ion by means of synthetic hydroxyapatite, Waste Manage. 22 (2002) 853–857.

E.D. Vega, J.C. Pedregosa, G.E. Narda, P.J. Morando, Removal of oxovanadium (IV) from aqueous solutions by using commercial crystalline calcium hydroxyapatite, Water Res. 37 (2003) 1776–1782.

I. Smiciklas, S. Dimovic, I. Plecas, M. Mitric, Removal of Co^{2+} from aqueous solutions by hydroxyapatite, Water Res. 40 (2006) 2267–2274.

B. Sandrine, N. Ange, B. Didier, C. Eric, S. Patrick, Removal of aqueous lead ions by hydroxyapatite: equilibria and kinetic process, J. Hazard. Mater. 139 (2007) 443–446.

R.R. Sheha, Sorption behaviour of Zn(II) ions on synthesized hydroxyapatites, J. Colloid Interface Sci. 310 (2007) 18–26.

S. Meenakshi, N. Viswanathan, Identification of selective ion exchange resin for fluoride sorption, J. Colloid Interface Sci. 308 (2007) 438–450.

X. Fan, D.J. Parker, M.D. Smith, Adsorption kinetics of fluoride on low cost materials, Water Res. 37 (2003) 4929–4937.

L.E.L. Hammari, A. Laghzizil, P. Barboux, K. Lahlil, A. Saoiabi, Retention of fluoride ions from aqueous solution using porous hydroxyapatite: structure and conduction properties, J. Hazard. Mater. 114 (2004) 41–44.

L.L. Hench, Biomaterials a forecast for the future, Biomaterials 19 (1998) 1419–1423.

P. Luo, Methods for synthesizing HA powders and bulk materials, US Patent 5858318, 1996.

M.G.S. Murray, J. Wanj, C.B. Ponton, P.M. Marquis, An improvement in processing of hydroxyapatite ceramics, J. Mater. Sci. 30 (1995) 3061–3074.

APHA, Standard Methods for the Examination of Water and Waste Water, American Public Health Association, Washington, DC, 2005.

Y.F. Jia, B. Xiao, K.M. Thomas, Adsorption of metal ions on nitrogen surface functional groups in activated carbons, Langmuir 18 (2002) 470–478.

W. Jie, L. Yubao, Tissue engineering scaffold material of nano-apatite crystals and polyamide composite, Eur. Poly. J. 40 (2004) 509–515.

C. Diaz-Nava, M.T. Olguin, M. Solache-Rios, Water defluoridation by Mexican heulandite-clinoptilolite, Sep. Sci. Tech. 37 (2002) 3109–3128.

F. Chen, Z. Wang, C. Lin, Preparation and characterization of nano-sized hydroxyapatite particles and hydroxyapatite/chitosan nano-composite for use in biomedical materials, Mater. Lett. 57 (2002) 858–861.

K.S. Low, C.K. Lee, A.C. Leo, Removal of metals from electroplating wastes using banana pith, Bioresource Technol. 51 1995) 227–231.

[24] A. Boualia, A. Mellah, T. Aissaoui, K. Menacer, A. Silem, Adsorption of organic matter contained in industrial H_3PO_4 onto bentonite: batch-contact time and kinetic study, Appl. Clay Sci. 7 (1993) 431–445.

[25] S. Meenakshi, Anitha Pius, G. Karthikeyan, B.V. Appa Rao, The pH dependence of efficiency of activated alumina in defluoridation of water, Indian. J. Environ. Prot. 11 (1991) 511–513.

[26] G. Karthikeyan, A. Shummuga Sundarraj, S. Meenakshi, K.P. Elango, Adsorption dynamics and the effect of temperature of fluoride at alumina-solution interface, J. Indian. Chem. Soc. 81 (2004) 461–466.

[27] G. Karthikeyan, Anitha Pius, G. Alagumuthu, Fluoride adsorption studies on montmoillonite clay, Indian J. Chem. Tech. 12 (2005) 263–272.

[28] H.M.F. Freundlich, Uber die adsorption in lösungen, Z. Phys. Chem. 57A (1906) 385–470.

[29] I. Langmuir, The constitution and fundamental properties of solids and liquids, J. Am. Chem. Soc. 38 (1916) 2221–2295.

[30] T.W. Weber, R.K. Chakravorti, Pore and solid diffusion models for fixed bed adsorbers, J. Am. Inst. Chem. Eng. 20 (1974) 228–238.

[31] O. Redlich, D.L. Peterson, A useful adsorption isotherm, J. Phys. Chem. 63 (1959) 1024.

[32] Y.S. Ho, Isotherms for the sorption of lead onto peat: comparison of linear and non-linear methods, Polish J. Environ. Stud. 15 (2006) 81–86.

[33] A.A. Khan, R.P. Singh, Adsorption thermodynamics of carbofuran on Sn(IV) arsenosilicate in H^+, Na^+ and Ca^{2+} forms, Colloid and Surf. 24 (1987) 33–42.

[34] M. Horsfall, A.I. Spiff, Effects of temperature on the sorption of Pb^{2+} and Cd^{2+} from aqueous solution by caladium bicolour (Wild Cocoyam) biomass, Electron. J. Biotechnol. 8 (2005) 162–169.

[35] Y.S. Ho, J.C.Y. Ng, G. McKay, Kinetics of pollutant sorption by biosorbents: review, Sep. Purif. Methods 29 (2000) 189–232.

[36] S. Lagergren, Zur Theorie der sogenannten adsorption geloster stoffe, K. Sven. Vetenskapsakad. Handl. 24 (1898) 1–39.

[37] Y.S. Ho, Second-order-kinetic model for the sorption of cadmium onto tree fern: a comparison of linear and non-linear methods, Water Res. 40 (2006) 119–125.

[38] Y.S. Ho, Citation review of Lagergren kinetic rate equation on adsorption reactions, Scientometrics 59 (2004) 171–177.

[39] M. Chanda, K.F. O'Driscoll, G.L. Rempel, Sorption of phenolics onto cross-linked poly (4-vinylpyridine), React. Polym. 1 (1983) 281–293.

[40] W.J. Weber, J.C. Morris, Equilibria and capacities for adsorption on carbon, J. Sanitary Eng. Div. 90 (1964) 79–107.

[41] Y. Önal, C. Akmil-Başar, D. Eren, Ç. Sarıcı-Özdemir, T. Depci, Adsorption kinetics of malachite green onto activated carbon prepared from Tunçbilek lignite, J. Hazard Mater. 128 (2006) 150–157.

[42] H.G. McCann, Reactions of fluoride ion with hydroxyapatite, J. Biol. Chem. 201 (1952) 247–259.

Defluoridation chemistry of synthesic hydroxyapatite at nano scale : Equilibrium and kinetic studies

1. 序論

飲料水の中のフッ化物はイオンは、健康に有害, 有益の両方の効果があることで知られています。

A1.5 ppm 以上の過度のフッ化物イオンを含む飲料水の消費は異なった形のフッ素症を引き起こします。水源からのフッ化物の除去は科学的にも実用的にも興味深い事です。飲料水に含まれるフッ化物は、イオン交換, イオン吸着または凝固作用, 沈殿現象によって取り除くことができます。これらのプロセスに基ずいて、幾つかのフッ素除去法が提案されました。提案された方法は、みょうばん, 石灰, アルミニウム, 硫酸, マグネシウム, 白雲石, 活性アルミナ, リン酸カルシウムなどの使用が必要となります。近年、逆浸透や電気透析, ナノフィルトレーション, donnan 透析, などの膜の過程は、水におけるフッ化物の濃縮を抑えるために調査されました。ナノ材料は新しい可能性を化学者に提供し、あらゆる面で化学がナノセケールで修正され変わる。表面特性, 電子構造, 化学配位 etc... は材料の次元がナノスケールに達したとき修正されるでしょう。そして目新しい化学はサイズの関数として発展するかもしれません。事実上表面サイトによる吸着で有毒化学物質を除去できるので、水からの有害化学物質の除去にナノ粒子を用いることができました。HAp 水処理の過程に広く用いられています。HAp を用いたカドミウム, オキソバナジウム, コバルト, 亜鉛, 鉛の除去が報告されています。従って本研究ではナノスケールで HAp のフッ化物除去能の研究を試みました。HAp を用いたフッ化物の除去は以前から報告されていましたが、HAp の使用が確実にフッ化物除去の分野で新しい寸法を与えるだろうと著者は感じた。よって HAp を用いてフッ化物除去実験を行いました。HAp はリン酸カルシウムをベースとしたバイオセラミックスで医療分野などに使われています。その理由は HAp は骨や歯などの生体硬組織の主成分だからです。HAp は沈殿法, ソルゲル, 熱水処理を含む様々なセラミックの過程で合成されます。その中で沈殿法は最も良い方法だと考えられます。その理由は実験法が非常に簡単で費用効率が良く、環境に優しいためユーザーにによって実験過程が用意に許容できるためだ。本研究では、HAp は実験室で沈殿法によって合成されました。そしてフッ素除去能の研究は、コンタクトタイム, 投与量, 他のイオンが DC に与える影響を細かく実験し、確実に HAp の DC メカニズムを理解しながらさらに注目されていくであろう、HAp の DC と動的運動の研究を徹底的にディスカッションしまた。

2. Materials and method

2.1 HAp の合成

HAp の合成はおおよそ 1.67 (Ca / P) 比の水酸化カルシウムとリン酸の反応による。反応

の pH レベルは 7.5 に維持されるべきだ。さもなければリン酸水素カルシウムの構成によるだろう。合成は 0.5 M の水酸化カルシウムの懸濁液を 1 h 加熱, 撹拌し, その間に酸を添加しました。0.3 M のリン酸溶液をゼリー状な沈殿物を作るために 40 ～ 42 ℃で 1 ～ 2 滴加えました pH はアンモニア水でコントロールした。そして得られた沈殿物を蒸留水で洗い 80 ℃で乾燥, 400 ℃で焼成して HAp パウダーを得られました。

2.3

フッ化ナトリウムの原液 (100 mg / L) を用意して、フッ化物の吸着に使いました。バッチ吸着実験は、初濃度 10 mg / L の溶液 50 mL に HAp 0.25 g を加え行われました。溶液は 200 rpm のスピードで回転するサーモスタッドシェーカーを使ってシントウした。次に溶液をフィルターにあえ残りのフッ化物イオンは、イオン分析器 A 940 とフッ化物イオンを測定する電極 BN 9609 を使って測定した。pH は pH メーターで測定。吸着の運動的, 熱力学的なパラメーターは、温度制御可能なシェーカーで 303, 313, 323 K で実験を行うことによって確立した。吸着剤の DC 能は、吸着剤の量を変えて様々な実験を行った。同様に最大の DC の値を求めるために、吸着剤の反応時間をいろいろ変えて実験したそして負のイオンが DC に与える影響を調べた。NO_3^- と SO_4^{2-} の濃度は分光光度計で測定した。他の水質のパラメーターは標準法で求めた。HAp の pHzpc は pH ドリフト法で測定し、micrcal origin ソフトウェアで計算した。復帰相関係数と決定係数を使って適合するかを議論した。

3.1

HAp を特徴づけるために XRD, FT-IR, TEM 分析を合成 HAp, フッ素処理後の合成 HAp について行った。クリスタルピーク 2θ =25.9, 32, 33, 35.5, 40 は HAp 特有のピークである。これらのピークはフッ素処理した後でも顕著な変化はみられなかった。これと類似した報告が Diaz – Nara らによってされている。Fig.2 a and b は FT-IR スペクトラ結果です。3570 cm^{-1} の結合は – OH 基の伸縮振動に属する。1040, 603, 566 cm^{-1} のピークはリン酸の伸縮, 変角振動です。フッ素処理後に突然現れたピークは-OH と F の水素結合です。HAp の TEM image は Fig.3 に示します。パウダーのサイズは 200 nm で円柱状の小枝のような形をしていて、粒子は均質なマイクロ構造で、規則正しいナノ材料を形づくっている。

3.2

フッ素イオンの吸着は 10 ～ 60 min の反応時間で」初濃度 10 mg / L, 室温で行われ, 反応時間との関係を示した。およそ 30 分で吸着は飽和状態となった。このことから反応は 30 min に固定した。しかし、n – HAp は飽和まで 30 分を要する。この事から除去過程は、イオン交換よりも遅い吸着によって制御されていると考えられる。N – HAp の最適な添加量を確立するために、添加量をいろいろ変えて実験したところフッ素除去のパーセント量は吸着剤の量を増やせば増やすほど高くなった。これはアクティブサイトが増えたためと考え

られる。

3.3

　溶液の pH は重要な役割を果たす。従って、HAp のフッ素吸着量を様々な pH の範囲で行いました。pH が高くなるにつれてフッ素除去量は減少していった。溶液の pH は HCl / NaOH でコントロールした。最大吸着量は pH 3 で 1845 mgF$^-$ / kg そして最も低かったのは pH 11 で 570 mgF$^-$ / kg だった。類似した結果が Karthikeyan らによって報告されている。活性アルミナを吸着剤として使ったとき、この事は吸着剤表面のチャージで説明できる。酸媒体中で表面は高い＋のチャージを持つことが確立されている。そして酸媒体中で最大 DC は一般に引力の増加による。アルカリ溶液中で DC が低くなっていくのはアルカリ表面のチャージが－のため、溶液とフッ素イオン双方が－のチャージをもつので反発しあうという事実によって説明できる。この論証は zero point charge によって支えられている。化学吸着は pHzpc 以下と以上の値で起こる。イオン交換に加えて物理吸着によるだろうことから DC メカニズムは、Scheme 1 – 3 で説明できる。

3.4

　HAp の DC は Cl$^-$, SO$_4^{2-}$, NO$_3^-$, HCO$_3^-$ の様な負のイオンが影響するという事が水の研究で証明されている。負のイオン濃度 100 ~ 500 mg/L でフッ素濃度を 10 mg/L に室温 30 ℃で実験した結果を Fig.8 に示す。混在した負のイオンが HAp の DC に与える影響を調べた。SO$_4^{2-}$, NO$_3^-$, HCO$_3^-$・Cl$^-$ は HAp の DC に大きな影響は与えないと推定する。しかし、HCO$_3^-$ は HAp の DC を 1290 ~856 mgF$^-$ / kg に減少させる。従って、HCO$_3^-$ は吸着する間に F$^-$ に張り合っていると考えられる。類似した結果が活性アルミナ, モンモリロナイト, 粘土のフッ素除去特性で報告されている。

3.5

　吸着等温泉は溶質の濃度と吸着剤表面にたまった蓄積物との関係を表す。HAp のフッ素吸着能を 3 つの異なった等温線で評価した。すなわち、langmuir, Freundlich, Redlich – peterson 等温線で評価した。線形形式を Table 1 に示す。

q$_e$ は吸着剤 1 g 当りのフッ素吸着量 (平衡状態)
C$_e$ はフッ素の残存濃度
K$_F$ は吸着能の限界値
1/n は吸着の強さ

定数 K$_F$ と n は log q$_e$ と log C$_e$ のグラフから、傾きと切片を計算することで求められ、その結果を Table 2 に示す。1 / n の値は 0.1 ~1.0 の範囲、n の値は 1 ~ 10 の範囲に収まると吸着

にとって有用な状態と決定づけられる。Langmuir のモデルは4タイプあり Table 1 に示す。吸着能 (Q°)は単層吸着での吸着量を示す。Q°は吸着剤の最大吸着量を示し、b は langmuir の吸着エネルギーとの関係である。それぞれ Q° と b の値は C_e / q_e のグラフの直線の傾きと切片から求められる。この結果を Table 2 に示す。等温線の実行可能性を調べるために、langmuir の特徴は分離要因、または平衡のパラメーターR_L によって表せる。

$R_L = 1 / 1 + bC_o$

b は langmuir の不変性を示す。
C_o はフッ素の初濃度を示す。

R_L の値は 0~1 で langmuir モデルから有用な吸着条件を求められる。Peterson は3つのパラメーターの等温線で langmuir と Freundlich 両方の特徴を持つ。等温線の A, B, δは trial and-error を使って Peterson の平衡から線を引いて評価できる。コンピューター操作に適切な trial and-error は ln[A (C_e / q_e)－1]における ln C_e の直線復帰のための A の一連の値を求めるために、回帰係数 (r)を測定して、r の最大の最適化された値とδのそれぞれんの値をもたらす A の最も良い値を得るために開発された。そして B は ln C_e と ln[A (C_e / q_e)－1]のプロットの傾きと切片から決定した。上記から langmuir のモデルに提案された等温線が近づいているのをδの値から見ることができる。

3.6 chi - square - test

□□□におけるフッ化物吸着の適切なモデルを特定するために、この分析が行われた。分散統計値テストは基本的に実験データとの違いの二乗の合計と、二乗されたモデルから計算することによって得た値が対応する。データが割られた、それぞれ違いのあるモデルから計算されたデータです。

計算式は $x^2 = \Sigma \ (q_e - q_{e,m})^2 / q_{e,m}$

$q_{e,m}$ はモデルから計算された平衡容量です。
q_e は平衡容量のための実験データです。

モデルノデータが実験データと一致するなら x^2 の値は小さくなるだろう。反対にモデルのデータと実験データが一致しないと x^2 の値は高くなるだろう。chi - square – test 結果を Table 2 に示す。

Langmuir 1 > Freundlich > 4 > 3 > 2 > Peterson

Langmuir 1 と Freundlich が良く適合すると評価され、最も優位な単分子化学吸着をしめすのは Langmuir 1 と考えられます。

3.7
吸着に関連づけられた熱力学的パラメーター

ΔG° 標準自由エネルギー変化
ΔH° 標準エンタルピー変化
ΔS° 標準エントロピー変化
Ea 活性化エネルギーは以下の通りに計算される。

$$\Delta G^{\circ} = -RT \ln K_{\circ}$$

吸着反応のための分配係数 $K_{\circ}$ は $\ln q_e / C_e$ と C_e のグラフの直線の傾きから決定される。そして zero C_e を推定する方法はカーンらによって示された。

T はケルビン温度で
R は気体の状態係数
吸着分配係数 $K_{\circ}$ は ΔH° と ΔS° で表せる。

$$\ln K_{\circ} = \Delta H^{\circ} / RT + \Delta S^{\circ} / R$$

ΔH° 標準エンタルピー変化
ΔS° 標準エントロピー変化

ΔH° の値として ΔS° は $\ln K_{\circ}$ と $1 / T$ のグラフの傾きと切片から求められる。修正された arrhenius – type の方程式は、表面被覆率 (θ) から与えられる S^{*} となる。S^{*} は吸着質 / 吸着性のシステムの機能です。このシステムは吸着質が吸着面に無限に残る可能性の基準です。

$$S^{*} = (1-\theta)\exp-(E_a / RT)$$
θ は表面被覆率で $\theta = (1 - C_e / C_{\circ})$ です。

$C_{\circ}$ は初濃度。
C_e は残存濃度を表す。

$1/T$ に対する $\ln S^{※}$ の切片と E_a / R の傾きを使って作ることができる。吸着過程の主要な影響要素の温度効果は Hap の吸着つまりは 3 つの異なった温度 303, 313, 323 K で最適化された状態で熱力学的なパラメーターでモニターされました。$\triangle G^{\circ}$, $\triangle H^{\circ}$, $\triangle S^{\circ}$ そして E_a は Eqs から求められる。(3)−(6)と $\triangle G^{\circ}$, $\triangle H^{\circ}$, $\triangle S^{\circ}$ は Table 3 に示す。$\triangle G^{\circ}$ の値がマイナスなので吸着の過程は、自然発生的であるということが示されるだろう。$\triangle H^{\circ}$ そして E_a が正の値という事は、吸着の過程で吸熱性を示します。正の数 S° はフッ化物イオン吸着の偶発性の増加を示します。$S^{※}$ が 0 に近い 0.1 なので、化学吸着に基づいて起こることがわかった。

3.8

大量輸送や化学反応のプロセスなど、吸着メカニズムを理解するために 2 つのモデル, 反応ベース, 拡散ベースのモデルをテストするために行った。バッチ吸着力学の予測がこの吸着を産業的に使うための柱となる。

3.8.1

フッ化物除去の吸着メカニズムを研究するために 1 次反応速度式, 2 次反応速度式の動的モデルは異なった実験条件で使用した。
簡易的な動的モデルの 1 次反応速度指揮は次式で表される。

$$\log q_e - q_t) = \log q_e - (Kad / 2.303)t$$

q_t は Hap の時間当たりのフッ素吸着量。
Kad は 2 次反応速度式の平衡速度定数です。
t に対する $\log q_e - q_t$ のグラフの直線は異なった実験条件のために一定の速度定数の値を与えるだろう。T に対する $\log q_e - q_t$ のグラフのプロットは直線を示すだろう。その直線は langmuir 方程式で適応性を示す。Table 4 に Kad と相関係数 r を示しました。1 次反応速度式モデルはより高い相関係数 r を示すため、実行可能であると考えられる。加えて 2 次反応速度式は広く使われる。4 つのタイプノ直線の 2 次反応速度式の動的なモデルがあります。一般的な 2 次反応速度式は次式で表される。

$$1 / q_t = 1 / h + t / q_e$$

$q_t = q_e^2 kt / (1 + q_e kt)$ は特定の時間の Hap 表面のフッ化物吸着量を示す。

K は 2 次反応速度式の速度定数です。
q_e は平衡状態で吸着されたフッ化物イオンと、はじめの吸着の吸着率です。

tに対する t / q_t のプロットから実験的に 2 次反応速度式の q_e, K, h を得ることができる。ま
た Hap におけるフッ化物の吸着の 2 次反応速度式モデルの適合性は分析されました。T / q
に対する t のプロットはより高い相関係数 r を与えます。1 次反応速度式のモデルが 2 次反
応速度式のモデルに対して適合性と値が Table 5 に示されています。初濃度の増加に伴って
q_e の値は増加しました。そしてまた、q_e の値は温度の増加によっても増加しました。また
温度は化学吸着を示していて、温度の増加に伴って速度定数の値 K も増加しました。直線
の分析では異なった線形形式の同じモデルはパラメーターの計算にかなり影響するでしょ
う。H_o によると、非線形のメソッドは運動のパラメーターを得るためによりふさわしい方
法であるだろう。非線形のメソットにおいてコンピューター操作に適切な試行錯誤手段は
マイクロソフトスプレットシートがある。ある解答者アドインを使用することで、実験デー
タと 2 次反応速度式モデルの間の決定係数 r^2 を最大にするために最適化ルーチンで 2 次
反応速度式パラメーターを決定するために開発されました。この研究で決定係数は e_q を使
用することで計算されました。直線的, 非線形の 2 次反応速度式運動が実験データにモデル
化する適合テストを以下の式で行った。

$$r^2 = \Sigma(q_m - q'_t)^2 / (q_m - q'_t)^2 - (q_m - q_t)^2$$

q_m は 2 次反応速度式の動的モデルから特定の時間 t で得ることができる。
q_t は Hap 表面のフッ化物イオン吸着量で実験から得られた q'_t は q_t の平均です。

決定係数 r^2 は線形, 非線形メソッドから計算できるそしてこれを Table 5 に示す。非線形メ
ソッドによる r^2 の q_e, K, h より高い値の実験データが Table 5 に示されており、非線形の 2
次反応速度式メソッドのよりよい適用性を示します。

3.8.2
個体-液体吸着の過程において、通常溶質転送は粒子拡散か気孔拡散で特徴づけられる。
粒子の拡散吸着制御の過程のための 1 次方程式は以下の通りである。

$$\ln(1 - C_t / C_e) = -K_p t$$

K_p は粒子速度定数です。

$\ln(1 - C_t / C_e)$ の傾きで、t に対して粒子速度定数の値を得ます。ここで使用された、気孔流行
伝播モデルはウェーバーとモリスによって提案された理論を示します。イントラップパー
ティクル拡散方程式を以下に示します。

$$q_t = K_i t^{1/2}$$

K_i はイントラップパーティクル速度定数です。

$t^{1/2}$ に対する q_t のプロットの傾きはイントラップパーティクル速度定数の値を与えます。q_t 対 $t^{0.5}$ のプロットが与える 2 つのメカニズムが、吸着過程に関わるのを示す最初の曲線を直線のあとの示す。直線的な部分がイントラップパーティクル拡散に対応している間のはじめの曲線は、境界層効果を表します。式 (10) と気孔流行伝播モデルの両方が適応されました。そして、K_p と K_i の値は Table 6 に示します。両方の場合におけるより高い r の値は、粒子と気孔流行伝播モデルの両方によって制御され吸着の過程の可能性を示します。

3.9

　スクエア・サム・オブ・エラーについて計算することによって、吸着データに採用している動的モデルの強化を行いました。SSE のしたの値は吸着データによりよく合うように吸着メカニズムの印を与えることができます。

$$SSE = \Sigma (q_{t,e} - q_{t,m}) / q^2_{t,e}$$

$q_{t,e}$ と $q_{t,m}$ は時間 t 当りのフッ化物の実験吸着容量を動的モデルから与えられる換算値です。反応ベースとして拡散ベースの動的なモデルの SSE 値は Table 7 に計算してまとめました。最も低い SSE 値を与えるノデルがこのシステムのための最高のモデルであると考え、次にこのモデルに基づいて吸着メカニズムを説明します。Table 7 から 2 次反応速度式、オデルと気孔流行伝播モデルが他の 2 つのモデルよりもよりよく適用されるという観測がされました。

3.10

HAp によるフッ化物除去は吸着とイオン交換メカニズムの両方によって制御されると考えられます。フッ素溶液中でならイオンは scheme 1 に示されるような形で Hap 表面に吸着されます。酸性の媒体中では H＋イオンの濃度が高く、したがって HAp 表面はより多くのフッ化物イオンを引きつける正帯電型を取得して、したがって pH が賛成になるとフッ素除去能が増加します。この反応を scheme 2 に示します。上記で説明した HAp とフッ化物イオンの間の引力は745 cm−1 に新しいピークが出ることを FT-IR の測定結果より確認したことにより裏付けられます。このピークはフッ化物吸着した事によって、HAp の OH と F が水素結合したことによってできる特徴的な振動です。PH の増加がゆっくり表面化するようにフッ化物イオンを退ける負帯電型を与えてください。そうすれば、静電気引力によるフッ化

物除去はアルカリ性の媒体で除去できます。また、イオン交換メカニズムは HAp によるフッ化物除去にかかわります。HAp の OH グループを荷電粒子であるとみなしてフッ化物イオンと交換できます。イオン交換による HAp のフッ素除去は scheme 3 に示す。したがって HAp によるフッ素除去はイオン交換と吸着メカニズムの両方によって起こると結論づけられる。その結果、それは有用なフッ化物除去剤としての役割をなすものと考えられる。

3.11

　現場で HAp の適用性をためすためフッ化物イオンが過剰な区域からサンプルを取りテストした。その結果を Table 8 に示す。HAp で処理した水の中のフッ素濃度は許容限界内に収まり、そして処理後に他のパラメーターにおける著しい変化は全くありませんでした。

...determined experimentally by S. T. Kim

...gradients in $\delta^{18}O$ of meteoric water were fit
...weighted annual mean precipitation and for
...monthly average (always in January or
...collected in 1984 and reported in (18).
...least-squares methods and second-order
...equations, and they fit data with r^2 values of
...both the annual weighted mean and the
...monthly average. These data were then
...measured altitude gradients in mean
...temperature and maximum monthly average
...temperature [also always in January or February (17–19)]
...the relationships between temperature and $\delta^{18}O$
...plotted as curves in Fig. 1.

...The slope in Fig. 1 defined by data for carbonate growth
...and parental waters is 0.34‰/°C. This is
...indistinguishable from the slope defined by the mean
...altitude gradient in surface temperature and $\delta^{18}O$
...meteoric water in the Altiplano and surrounding area
...(17–19) and contrasts with slopes in these
...associated with low-latitude climate variations
...(–2‰/°C for temperatures between 29° and 12°C),
...altitude variations (–3‰/°C or 0.6‰ per degree of
...or seasonality at any one altitude [~ –5‰/°C
...varying with altitude; see (18) and dashed lines in
Fig. 1]. For data documenting these trends, see (44).
A. G. Smith, A. M. Hurley, J. C. Briden, Phanerozoic
Paleocontinental World Maps (Cambridge University
Press, Cambridge, 1981).

24. S. M. Savin, R. G. Douglas, F. G. Stehli, Geol. Soc. Am.
Bull. 86, 1499 (1975).
25. J. Zachos, M. Pagani, L. Sloan, E. Thomas, K. Billups,
Science 292, 686 (2001).
26. C. N. Alpers, G. H. Brimhall, Geol. Soc. Am. Bull. 100,
1640 (1988).
27. G. D. Hoke, B. L. Isacks, T. E. Jordan, J. S. Yu, Geology 32,
605 (2004).
28. B. K. Horton, Tectonics 18, 1292 (1999).
29. B. Liu, F. M. Phillips, A. R. Campbell, Palaeogeogr.
Palaeoclimatol. Palaeoecol. 124, 233 (1996).
30. T. E. Cerling, J. Quade, in Continental Indicators of
Climate, Proceedings of Chapman Conference, Jackson
Hole, Wyoming, P. Swart et al., Eds. [American
Geophysical Union (AGU) Monograph 78, AGU,
Washington, DC, 1993], pp. 217–231.
31. Crustal shortening accompanied by isostatic compensation
of thickened crust leads to elevation change by the
relation $\partial H/\partial T = \partial U/\partial T \times Z/W \times [(\rho_c - \rho_a)/\rho_a]$, where
$\partial H/\partial T$ is the rate of elevation gain, $\partial U/\partial T$ is the shortening
rate (10 mm/year, based on long-term plate motions), Z is
the initial crustal thickness (50 km), W is the width of the
deforming region (300 km), ρ_c is the density of the crust
(assumed to equal 2.7 g/cc), and ρ_a is the density of the
mantle (assumed to equal 3.3 g/cc). See (15) for
explanations of these choices of values for the physical
constants. This relation predicts a maximum rate of
elevation gain that is, not considering any elevation losses
due to erosion) of 0.3 mm/year.
32. P. Bird, J. Geophys. Res. 83, 4975 (1978).

33. P. C. England, G. Houseman, J. Geophys. Res. 94, 17561
(1989).
34. R. W. Kay, S. Mahlburg-Kay, Geol. Rundsch. 80, 259 (1991).
35. S. Lamb, L. Hoke, Tectonics 16, 623 (1997).
36. L. Echavarria, R. Hernandez, R. Allmendinger, J. Reynolds,
AAPG Bull. 87, 965 (2003).
37. P. Ghosh et al., Geochim. Cosmochim. Acta, in press.
38. J. M. McCrea, J. Chem. Phys. 18, 849 (1950).
39. P. K. Swart, S. J. Burns, J. J. Leder, Chem. Geol. 86, 89
(1991).
40. J. M. Eiler, E. A. Schauble, Geochim. Cosmochim. Acta 68,
4767 (2004).
41. H. Affeck, J. M. Eiler, Geochim. Cosmochim. Acta, in
press.
42. Z. Wang, E. A. Schauble, J. M. Eiler, Geochim. Cosmochim.
Acta 68, 4779 (2004).
43. S. T. Kim, J. R. O'Neil, Geochim. Cosmochim. Acta 61,
3461 (1997).
44. J. R. Gat, W. G. Mook, H. A. J. Meijer, Environmental
Isotopes in the Hydrological Cycle: Principles and
Applications. Volume II: Atmospheric Water (IAEA, Vienna,
Austria, 2001); available at www.iaea.org/programmes/
ripc/ih/volumes/volume2.htm.
45. K. M. Gregory-Wodzicki, Geol. Soc. Am. Bull. 112, 1091
(2000).
46. K. M. Gregory-Wodzicki, W. C. McIntosh, K. Velasquez,
Am. Earth Sci. 11, 533 (1998).

Freezing as a Path to Build Complex Composites

Sylvain Deville,* Eduardo Saiz, Ravi K. Nalla,† Antoni P. Tomsia

Materials that are strong, ultralightweight, and tough are in demand for a range of applications, requiring architectures and components carefully designed from the micrometer down to the nanometer scale. Nacre, a structure found in many molluscan shells, and bone are frequently used as examples for how nature achieves this through hybrid organic-inorganic composites. Unfortunately, it has proven extremely difficult to transcribe nacre-like clever designs into synthetic materials, partly because their intricate structures need to be replicated at several length scales. We demonstrate how the physics of ice formation can be used to develop sophisticated porous and layered-hybrid materials, including artificial bone, ceramic-metal composites, and porous scaffolds for osseous tissue regeneration with strengths up to four times higher than those of materials currently used for implantation.

Although the potential of layered materials has long been recognized (1), their creation requires solving a two-fold problem, namely the design of optimum microstructures and the development of fabrication procedures to implement these designs. Natural materials such as nacre offer a wealth of information to guide such a design process (2, 3). The unique properties of natural layered materials are achieved through fine control of the layer thickness, selection of the right components, and manipulation of roughness and adhesion at the organic-inorganic interface

(4, 5). The ideal fabrication process has to be not only simple but also adaptable enough to fabricate layers with a large number of material combinations and a wide range of layer dimensions. Previous techniques for mimicking nacre are bottom-up chemical approaches (6, 7) that are intrinsically limited to a narrow range of materials exhibiting the proper interfacial reactions and compatibility. Other techniques offer only a coarse control of the layer thickness or have practical limitations regarding the number of layers that can be fabricated (7, 8).

In sea ice, pure hexagonal ice platelets with randomly oriented horizontal c crystallographic axes are formed, and the various impurities originally present in sea water (salt, biological organisms, etc.) are expelled from the forming ice and entrapped within channels between the ice crystals (9). We apply this natural principle to ceramic particles dispersed in water to

build sophisticated, nacre-like architectures in a simple, two-step approach. Ice-templated (IT), porous, layered materials with layers as thin as 1 μm are first fabricated through a freeze-casting process, which involves the controlled unidirectional freezing of ceramic suspensions. These porous scaffolds are then filled with a selected second phase (organic or inorganic) to fabricate dense composites. By using a natural, self-organizing phenomenon, we allow nature to guide the design and processing.

The physics of water freezing has drawn the attention of scientists for a long time. With few exceptions (10), much of this work has concentrated on the freezing of pure water or very dilute suspensions (9, 11). This phenomenon is critical for various applications, such as cryo-preservation of biological cell suspensions (12) and the purification of pollutants (13). An important observation in these studies is that, during the freezing of such suspensions, there is a critical particle size (11) above which the suspended particles will be trapped by the moving water-ice front. Another important observation is that the hexagonal ice crystals exhibit strong anisotropic growth kinetics, varying over about two orders of magnitude with crystallographic orientation. Under steady-state conditions, it is possible to grow ice crystals in the form of platelets with a very high aspect ratio. The ice thus formed will have a lamellar microstructure, with the lamellae thickness depending mainly on the speed of the freezing front. We designed a simple experimental setup (fig. S1) that allowed us to precisely control the freezing kinetics. By freezing concentrated suspensions containing ceramic particles with suitable granulometry, we were

Materials Sciences Division, Lawrence Berkeley National
Laboratory, Berkeley, CA 94720, USA.

†Present address: Intel Corporation, 5000 West Chandler
Boulevard, Chandler, AZ 85226, USA.

*To whom correspondence should be addressed. E-mail:
apromsia@lbl.gov
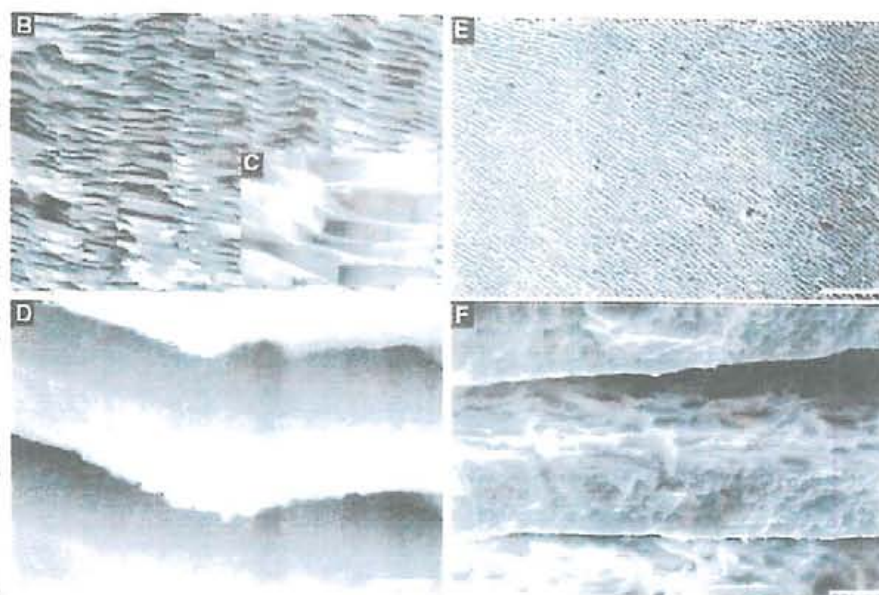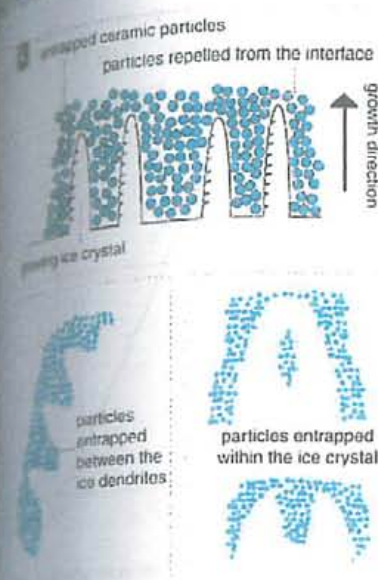
Fig. 1. Processing principles and materials. While the ceramic slurry is freezing, the growing ice crystals expel the ceramic particles, creating a lamellar microstructure oriented in a direction parallel to the movement of the freezing front (A). For highly concentrated slurries, the interaction between particles becomes critical: A small fraction of particles are entrapped within the ice crystals by tip-splitting and subsequent healing (B), leading to the formation of inorganic bridges between adjacent walls. Dense composites are obtained by infiltrating the porous lamellar ceramic with a second phase (e.g., a polymer or a liquid metal). Natural nacre has a brick-mortar-bridges microstructure where inorganic calcium carbonate layers are held together by organic protein "glue" (B and C); the roughness of the inorganic walls (D) is a key contributor to the final mechanical properties of nacre. The layered microstructure of the IT dense composites resembles that of nacre [for example, the alumina–Al-Si composite in (E)]. The particles entrapped between the ice dendrites generate a characteristic roughness on the lamella surface (F) that mimics that of the inorganic component of nacre. Scale bars indicate (B) 5 μm, (C) 0.5 μm, (D) 0.3 μm, (E) 300 μm, and (F) 10 μm.
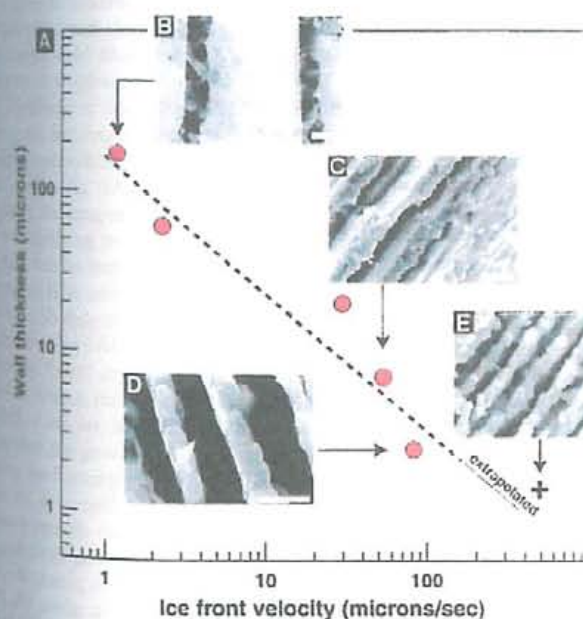
Fig. 2. Microstructural control at several levels. (A) Effect of the speed of the solidification front on the thickness of the lamellae for alumina samples fabricated from powders with an average grain size of 0.3 μm (B to E). The scanning electron micrographs shown in the graph correspond to cross sections parallel to the direction of movement of the ice front. Sample (E) was obtained with ultrafast freezing to gauge the thickness limit achievable by this technique. The approximate ice front velocity for this extreme case is in agreement with the extrapolation of the controlled freezing results. In addition, it is possible to control the materials mesostructure, for example in alumina (F), by patterning the surface of the cold fingers on which the ice crystals grow. Scale bars indicate (B) 50 μm, (C) 10 μm, (D) 5 μm, (E) 5 μm, and (F) 500 μm.
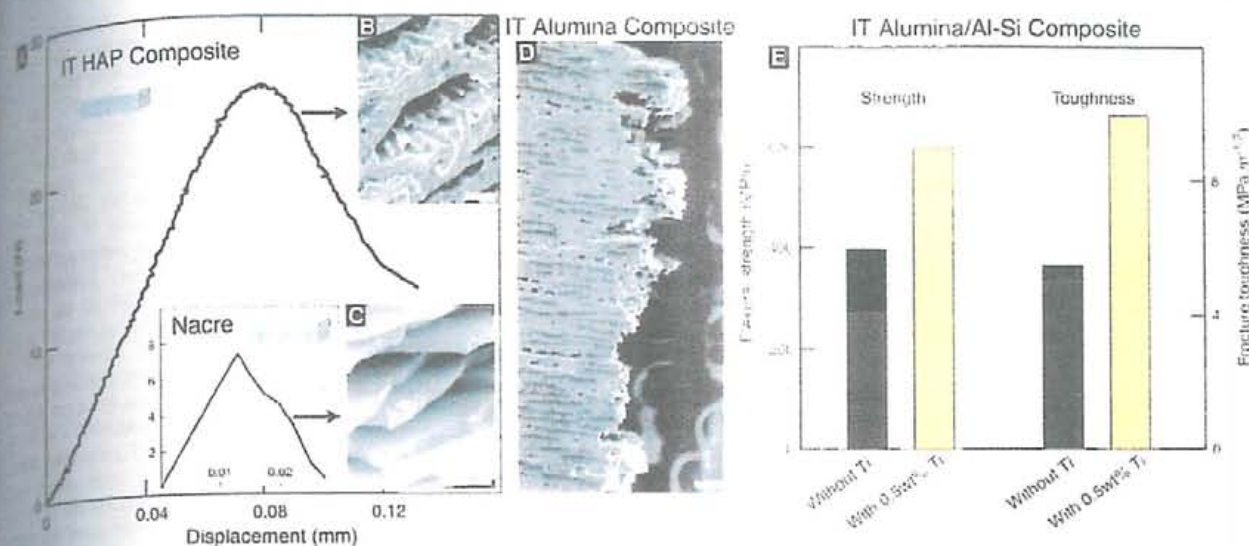
Fig. 3. Mechanical response of natural and synthetic IT composites. The three-points bending load-displacement data for IT HAP-epoxy compos- ite (A) was qualitatively very similar to that of nacre (C) (17), with a gradually decreasing load after the elastic limit—characteristic of a stable crack propagation and active toughening—for cracks propagating in the direction perpendicular to the inorganic layers. Typical scanning electron micrographs of the IT composites (B) and nacre of abalone shell (C) reveal similar features on the fracture surface, with mode I cracks moving away from the notch and deflecting at the lamellae. Extensive crack deflection at the organic-inorganic interface results in tortuous crack paths and contributes to the toughening in both cases [as can be observed for the IT alumina-epoxy composite in (D)]. The role of the interfacial chemistry in the bonding between layers and the final mechanical properties of the material is illustrated in the data (E) for alumina–Al-Si composites (45/55 vol %); the addition of 0.5 wt % titanium to the aluminum alloy significantly increases the strength and toughness of the materials. Scale bars indicate (B) 40 μm, (C) 1 μm, and (D) 100 μm.

to build homogeneous, layered, porous solids.

In the method proposed here (Materials and methods), directional freezing of the ceram- ic slurries is achieved by pouring them into polytetrafluoroethylene molds placed between two copper cold fingers (fig. S1) whose tem- perature is regulated to control the speed of the solidification front (fig. S2). As in nature, during the freezing of sea water, the ceramic particles concentrate in the space between the ice crystals (Fig. 1A). When the freezing rate increases, the magnitude of supercooling ahead of the solidifying interface is increased, and as a result the tip radius of the ice crystals de- creases. A finer microstructure is thus obtained without affecting the long-range order of the structure. Afterwards, the ice is subli- mated by freeze drying, such that a ceramic scaffold whose microstructure is a negative replica of the ice is produced (Fig. 1F). We controlled the growth of lamellar ice by ad- justing the freezing kinetics. In this way, we obtained a layered microstructure with rele- vant dimensions that vary over two orders of magnitude (Fig. 2A) from 1 μm (almost the same as nacre, typically ~0.5 μm) (14) to 200 μm while affecting the ordered archi- tecture. To a large extent, the mesostructure of natural materials determines their mechan- ical response (15), and this mesostructure has been difficult to replicate synthetically. Our results indicate that, by controlling the freezing kinetics and patterns of the cold finger, it is

also possible to build mesostructural features and gradients (Fig. 2F) that could optimize the mechanical response of the final materials, for example, by stiffening the structure and lim- iting torsion (15).

The IT porous scaffolds obtained by this process exhibit strong similarities to the meso- and microstructure of the inorganic component of nacre (Fig. 1, B and C). The inorganic layers are parallel to each other and very homoge- neous throughout the entire sample (Fig. 1E). Particles trapped in between the ice dendrites (Fig. 1A) lead to a dendritic surface roughness of the walls (Fig. 1F), just as in nacre (Fig. 1D) (16). Lastly, some dendrites span the channels between the lamellae (Fig. 2B), mimicking the tiny inorganic bridges linking the inorganic platelets of nacre, which are believed to in- crease the fracture resistance (17).

The inorganic portion represents 95% of the volume of nacre, but its highly specific properties (in particular its great toughness) are due to the interaction of this inorganic com- ponent with the organic phase (protein) that is found between the calcium carbonate platelets (14). To obtain similar synthetic materials, we next filled the porous ceramic scaffolds with a second phase. For example, we filled the IT scaffolds with a simple organic phase (epoxy) or with an inorganic component (metal) (Fig. 1E). Nature shows that the optimum fracture properties are encountered not only when the organic/inorganic interface is strong but also when delamination at the organic/inorganic

interface occurs before the crack goes across the stiff, brittle layer. In the IT composites, extensive crack deflection at the interface be- tween layers was observed (Fig. 3, B and D). As in nacre (Fig. 3C), this delamination creates tortuous cracks that propagate in a stable man- ner (Fig. 3A) and increases the toughness of the materials. It is believed that nature manip- ulates adhesion in two ways, mechanical and chemical. In nacre, this is done by controlling the roughness and the highly specific properties of the polymer adhesive phase (4). Our process allows us to control the morphology of the inorganic layers and the chemistry of the inter- face. For example, the mechanical response of alumina–Al-Si [45/55 volume (vol) %] layered composites (Fig. 1E) can be manipulated by controlling the interfacial bonding. By adding as little as 0.5 weight (wt) % Ti [known to segregate at the metal-ceramic interfaces (18)] to the aluminum eutectic, the strength increases from 400 to 600 MPa and fracture toughness increases from 5.5 to 10 MPa/m^2 (Fig. 3E).

Our technique shows promise for a large number of applications that require tailored composite materials. One such scientific chal- lenge that could be solved is the development of new biomaterials for orthopedic applications (19). Despite extensive efforts in the develop- ment of porous scaffolds for bone regenera- tion, all porous materials have an inherent lack of strength associated with porosity. By ap- plying freezing to commercial hydroxyapatite (HAP, the mineral component of bone) powder

Fig. 4. Compressive strength of porous HAP scaffolds. Results versus literature [blue stars (22), green stars (23), inverted green triangles (24), black triangle (25), blue circle (26), inverted red triangle (27), diamonds (28), green triangle (27), diamonds (28), green triangle (27), and red circles (29)] versus IT porous HAP scaffolds. The typical pore sizes in conventional porous HAP scaffolds are on the order of 200 to 800 μm in order to allow bone ingrowth. In the IT materials exhibiting the greatest strength, the pores are typically 20 to 30 by ~200 μm wide and several millimeters long; previous studies have indicated that these dimensions are adequate for bone tissue engineering (20). For the IT porous materials, compression is ap-

plied in the direction parallel to the ceramic layers. The presence of inorganic bridges between the ceramic layers (a feature that parallels the microstructure of nacre) prevents Euler buckling of the ceramic layers and contributes to the high strength. (Inset) Typical compression load-displacement curves for materials with 56% porosity (three different samples shown here). The samples fail gradually, and, because of the large degree of control of hierarchical architecture, the mechanical behavior is very consistent from one sample to another.
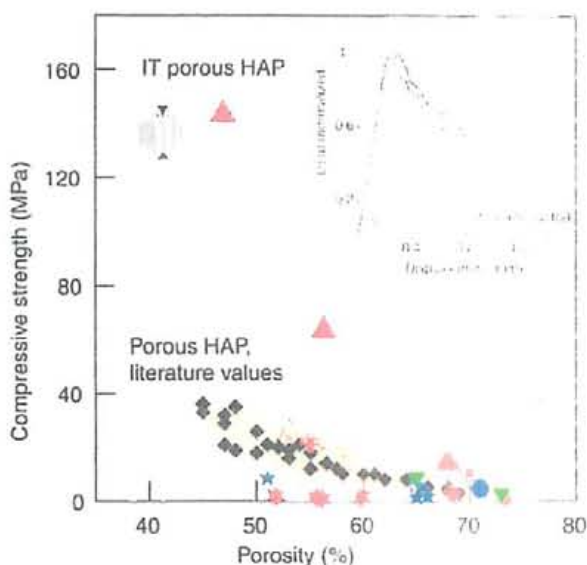
conditions, we processed IT highly porous lamellar scaffolds that are four times stronger in compression than conventional porous HAP (Fig. 4). These IT scaffolds exhibit well-defined pore connectivity along with directional and completely open porosity of an adequate size to allow bone ingrowth (20). Hence, most of the current shortcomings (low strength, random orientation, multiple pore size, and uncontrolled pore connectivity) that plague bone substitutes are eliminated by this innovative approach.

Current ceramic and metallic implant materials have serious shortcomings because of the mismatch of physical properties with those of bone. In bone, intrinsically weak materials, such as calcium phosphates and collagen, are combined into composites exhibiting intermediate modulus (10 to 20 GPa), fairly high strength (to 200 MPa), and high work of fracture (to 1000 J/m²) (21). The unique properties of bone arise from the controlled integration of the organic (collagen) and inorganic (mineral) components (5) with a sophisticated structure from the nano- to mesolevels. Our approach to the problem is to infiltrate the IT porous HAP scaffolds with a second organic phase with tailored biodegradability. Because the biodegradation rates of the scaffold and the infiltrated compound can be designed to be different, porosity can be created in situ to allow bone ingrowth. By using this approach, we have been able to fabricate HAP-based composites with stiffness (10 GPa), strength (150 MPa), and work of fracture (220 J/m²) that match compact bone for an equivalent mineral/organic content (around 60/40 vol %).

References and Notes

1. G. Mayer, Science 310, 1144 (2005).
2. C. Sanchez, H. Arribart, M. M. G. Guille, Nat. Mater. 4, 277 (2005).
3. L. Addadi, S. Weiner, Nature 389, 912 (1997).
4. B. L. Smith et al., Nature 399, 761 (1999).
5. G. E. Fantner et al., Nat. Mater. 4, 612 (2005).
6. Z. Y. Tang, N. A. Kotov, S. Magonov, B. Ozturk, Nat. Mater. 2, 413 (2003).
7. A. Sellinger et al., Nature 394, 256 (1998).
8. W. J. Clegg, Science 286, 1097 (1999).
9. M. G. Worster, J. S. Wettlaufer, J. Phys. Chem. B 101, 6132 (1997).
10. S. W. Sofie, F. Dogan, J. Am. Ceram. Soc. 84, 1459 (2001).
11. H. Ishiguro, B. Rubinsky, Cryobiology 31, 483 (1994).
12. J. O. M. Karlsson, Science 296, 655 (2002).
13. G. Gay, M. A. Azouni, Cryst. Growth Des. 2, 135 (2002).
14. A. P. Jackson, J. F. V. Vincent, R. M. Turner, Proc. R. Soc. Lond. Ser. B 234, 415 (1988).
15. J. Aizenberg et al., Science 309, 275 (2005).
16. R. Z. Wang, Z. Suo, A. G. Evans, N. Yao, I. A. Aksay, J. Mater. Res. 16, 2485 (2001).
17. F. Song, A. K. Soh, Y. L. Bai, Biomaterials 24, 3623 (2003).
18. E. Saiz, R. M. Cannon, A. P. Tomsia, Acta Mater. 48, 4449 (2000).
19. L. L. Hench, J. M. Polak, Science 295, 1014 (2002).
20. T. Dutta Roy, J. L. Simon, J. L. Ricci, E. D. Rekow, V. P. Thompson, J. R. Parsons, J. Biomed. Mater. Res. 66A, 283 (2003).
21. Y. H. An, in Mechanical Testing of Bone and the Bone-Implant Interface (CRC Press, Boca Raton, FL, 2000), pp. 41–63.
22. A. Almirall et al., Biomaterials 25, 3671 (2004).
23. R. P. del Real, J. G. C. Wolke, M. Vallet-Regi, J. A. Jansen, Biomaterials 23, 3673 (2002).
24. Y. Ota, T. Kasuga, Y. Abe, J. Am. Ceram. Soc. 80, 225 (1997).
25. A. Bignon, thesis, National Institute of Applied Science, Lyon, France (2002).
26. H. R. Ramay, M. Q. Zhang, Biomaterials 24, 3293 (2003).
27. M. Sous et al., Biomaterials 19, 2147 (1998).
28. D. M. Liu, Ceram. Int. 23, 135 (1997).
29. M. Milosevski, J. Bossert, D. Milosevski, N. Gruevska, Ceram. Int. 25, 693 (1999).
30. M. Kawata et al., J. Mater. Sci. Mater. Med. 15, 817 (2004).
31. This work was supported by the NIH National Institute of Dental and Craniofacial Research under grant 5R01 DE015633 ("Complex nanocomposites for bone regeneration") and by the Director, Office of Science, Office of Basic Energy Sciences, Division of Materials Sciences and Engineering of the U.S. Department of Energy under contract DE-AC03-76SF00098 (Metal/Ceramic Composites). The authors wish to thank R. O. Ritchie for useful discussions and J. Wu for help with the synthesis of the aluminum-infiltrated composites.

The Cellular Basis of a Corollary Discharge

James F. A. Poulet[1,2*] and Berthold Hedwig[2]

How do animals discriminate self-generated from external stimuli during behavior and prevent desensitization of their sensory pathways? A fundamental concept in neuroscience states that neural signals, termed corollary discharges or efference copies, are forwarded from motor to sensory areas. Neurons mediating these signals have proved difficult to identify. We show that a single, multisegmental interneuron is responsible for the pre- and postsynaptic inhibition of auditory neurons in singing crickets (Gryllus bimaculatus). Therefore, this neuron represents a corollary discharge interneuron that provides a neuronal basis for the central control of sensory responses.

An animal's behavior generates a constant flow of sensory information that can update or fine-tune ongoing motor activity (1) but can also desensitize the animal's own sensory pathways and/or be confused with external stimuli. One solution to these problems is to forward a signal, or corollary discharge, from motor to sensory regions during behavior to counter the expected, self-generated sensory feedback (2, 3). A role for corollary discharges

Biomimetic synthesis of hybrid nanocomposite scaffolds by freeze-thawing and freeze-drying

S NAYAR*, A K PRAMANICK, A GUHA, B K MAHATO, M GUNJAN and A SINHA

National Metallurgical Laboratory, Jamshedpur 831 007, India

Abstract. The aim of this study is to biomimetically synthesize hydroxyapatite–hydrophilic polymer scaffolds for biomedical applications. This organic–inorganic hybrid has been structurally characterized and reveals a good microstructural control as seen by the SEM analysis and the nanosize of the particulates is confirmed by AFM microscopy. The characterization of such nano-structured composites would allow researchers to design new systems, tailoring properties for different applications.

Keywords. Biomimetics; nanocomposites; hydroxyapatite; scaffolds; hydrophilic polymers.

1. Introduction

One of the most important issues in the synthesis of nanoparticles is knowing how to regulate the particle size and morphology. Biomimetics, a concept derived from Mother Nature and implemented in the design and synthesis of nanoscale materials, has been successful in creating functional nanomaterials and structures (Sinha et al 2001). Biomimetic synthesis realizes an in situ nucleation and growth of inorganic nanoparticles in a pre-organized organic matrix (Mann and Ozin 1996). The microstructural sophistication thus achieved by interfacial interactions provides much better functional properties than mere polymer–inorganic blends. It is established that different hydrophilic polymers can be used as pre-organized matrices in the biomimetic synthesis of a wide range of nanosystems including polymer–inorganic nanocomposites for tissue engineering (Sinha et al 2003). Here, we have used poly (vinyl) alcohol (PVA). Owing to its chemical composition very similar to the major component of human bone, hydroxyapatite (HAp) reinforced polymer nanocomposites are increasingly used as implants for medical applications (Nayar and Sinha 2004; Dorozhkin 2007). In the synthesis of HAp in PVA not only overcomes the poor mechanical properties of HAp but also provides a range of possibilities to create different forms of hybrid scaffolds for bone and cartilage grafts (Sinha et al 2007). The molecular recognition in these hybrid materials not only controls the shape and dimensions of HAp nanoparticles, yet assembles them into higher dimensional structures. In this paper, we describe how after the same initial biomimetic-synthesis of HAp in PVA, two different post-synthesis processing techniques lead to two different scaffold forms. A two-dimensional flat sheet after freeze-

drying and a three-dimensional block after repeated cycles of freeze thawing are formed. Both scaffolds were characterized by X-ray diffractometry (XRD), scanning electron microscopy (SEM) and atomic force microscopy (AFM).

2. Experimental

Biomimetic synthesis of HAp in PVA was established in our laboratory and the process patented by our group (Sinha et al 2005). In order to get 2-D fabric and 3-D block forms, we integrated this process with low temperature phase separation, achieved by freeze-drying and freeze-thawing, the patent of which is under way. In lyophilization, the temperature was drastically dropped to about −80°C whereas in freeze-thawing there were repeated cycles of freezing–thawing wherein water was entrapped and retained in the system. The chemicals were obtained from the following sources: PVA was from Qualigens with a molecular weight, 1, 25000, Ca (NO₃)₂ tetrahydrate from Hi Media and (NH₄)₂HPO₄ from Merck. While in freeze drying, the final slurry was dried at −80°C at a very fine vacuum of 0·03 milli bar for 36–48 h and packed and in freeze-thawing the synthesized slurry was kept in the freezer (4°C) of a frost free refrigerator. It was frozen and then thawed at room temperature. This thermal cycling was repeated on an average about 15 times whereby a nice hydrogel was obtained.

3. Results and discussion

Bone is a hierarchical nanocomposite built from ceramic tablets and organic binders, and is therefore, a subject of immense interest for materials scientists. PVA is a well-known hydrophilic biocompatible polymer and here we have capitalized on its ability to in situ synthesize HAp
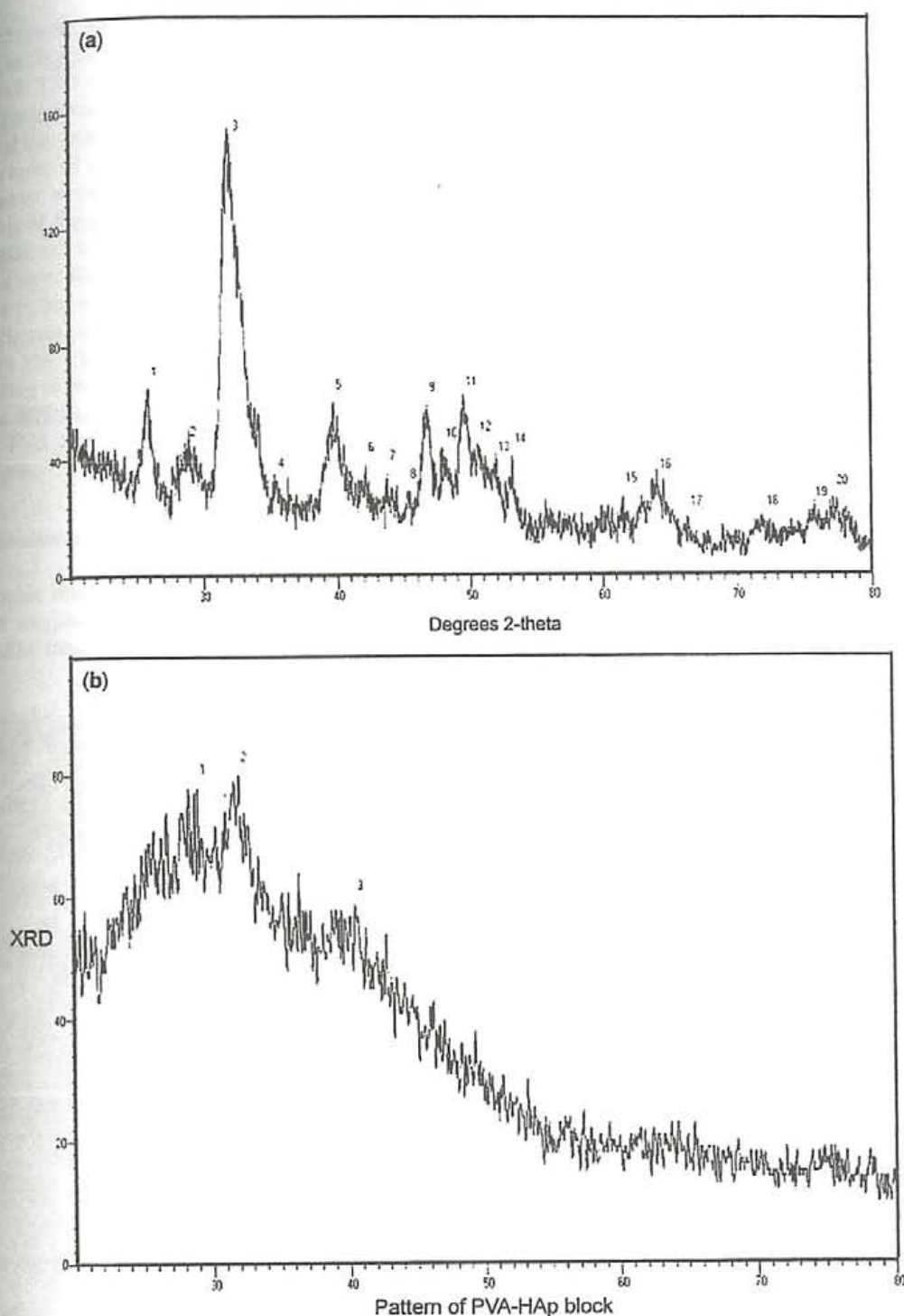
*Author for correspondence (nayar@nmlindia.org)

Figure 1. XRD patterns of (a) PVA–HAp sheet and (b) PVA–HAp block.

and physically cross-link itself under subjected condi-
tions. The XRD studies of both the scaffolds (the sheet
and the block) forms revealed HAp as the predominant
phase with the following characteristic peaks (210), (112),
(310), (221) and (113) for bandage and (210), (112) and
(221) peaks for block (figure 1). An appreciable degree of
crystallinity present in the PVA–HAp nanocomposites is
attributed to the surface energy of the organic surface which

as a nucleation catalyst, however, the growth remains limited due to sluggish diffusion process in polymer matrix. The block XRD data shows less crystallinity because of the entrapped water molecules. The SEM micrographs clearly reveal that both the scaffolds are made up of non-woven structures of cross-linked PVA–HAp nanofibrils having diameter in the range of 100–150 nm (figure 2). TEM analysis of the sample confirmed that PVA nanofibrils are highly mineralized with HAp nanoparticles (figure 3a). The sheet like nanocomposite revealed the HAp particle size to be about ~ 10 nm, however, a relatively larger particle size (80–100 nm) is obtained in PVA–HAp block (figure 3b). This seems to be logical as prolonged thermal cycling of biomimetic PVA–HAp provides ample time for the diffusion necessary for the growth of HAp particles in PVA matrix, hence, the size of the particles appears bigger.

3.1 *AFM studies in non-contact mode*

The topographic images reveal the particle-tip interaction and not the morphology. In compliance with the TEM data, the AFM images reveal an apparent clustering or

growth in the freeze-thawed sample in comparison with the lyophilized one. It also reflects the narrow size distribution of the synthesized HAp particles (figures 4a and b).

Scaffolds used in tissue engineering mimic the natural extracellular matrix and provide support for cell adhesion, migration and proliferation. Though our initial biocompatibility tests before the post-synthesis processing are as per standard norms, we are in the process of making these scaffolds in bulk in order to get the tissue specific cell-adhesion tests done.

4. Conclusions

The results shown here provide an excellent illustration of the symbiotic relationship that nanotechnology shares with innate polymer chemistry whether it is synthetic or biopolymers. We have initiated scaffold synthesis using HAp, PVA and collagen in both the sheet and block and the results are very encouraging. In polymeric systems, nanostructures play the role of nonreactor for growing nanoparticles. These materials are not only simple and cheap; they even control particles growth. Though our
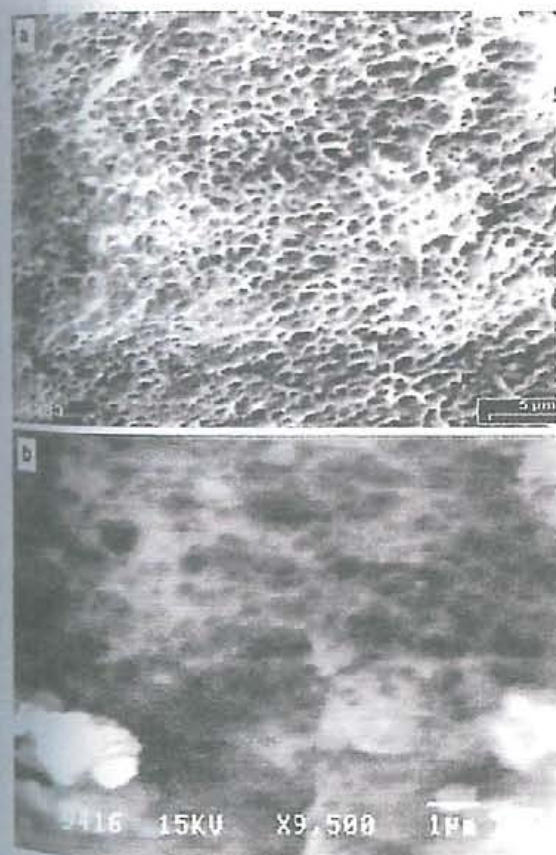

Figure 2. SEM micrographs of a. PVA–HAp nanocomposite sheet and b. PVA–HAp nanocomposite block.
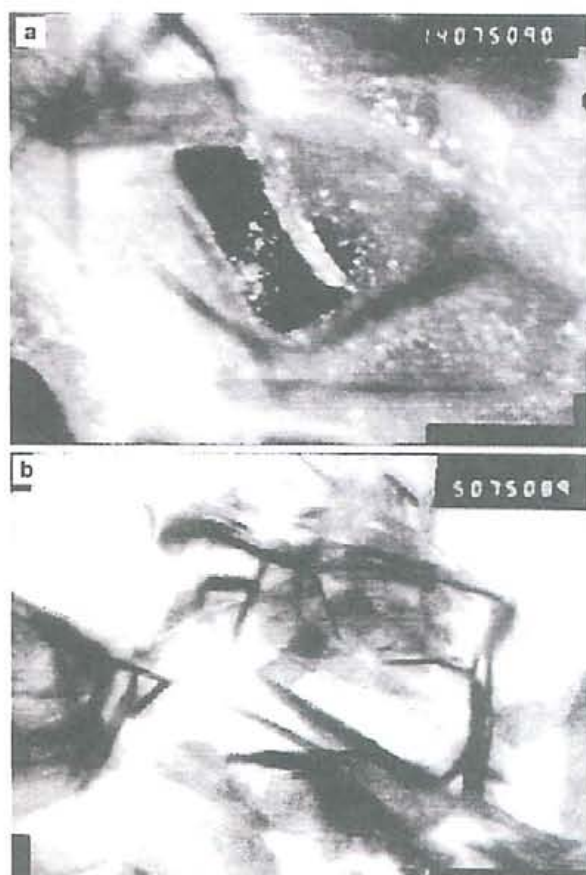
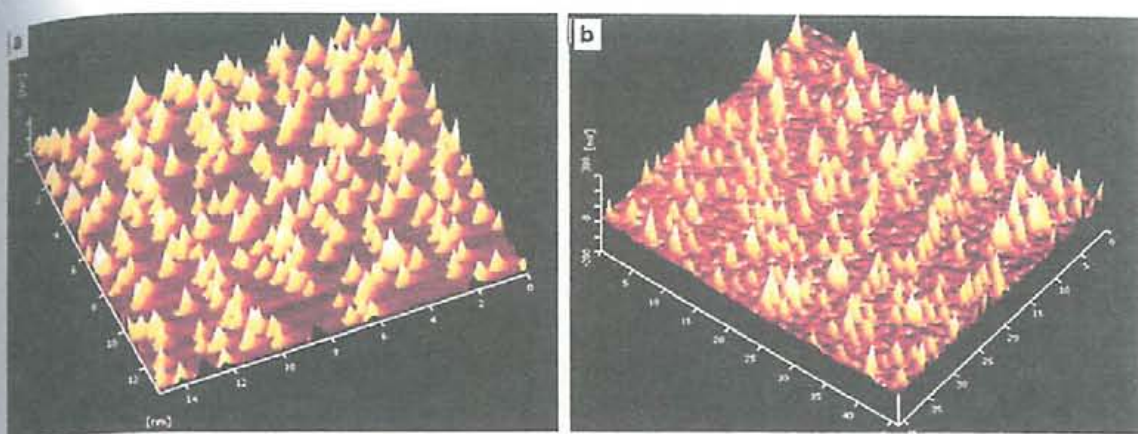**Figure 3.** TEM images revealing precipitation of HAp nanoparticles in a. PVA sheet and b. PVA block.

Figure 4. AFM topography revealing nanosized HAp particles in a. PVA sheet and b. PVA block.

results show improved microstructural and mechanical properties, for ideal tissue engineering, the desired tissue should be used as the model to engineer the chemical, mechanical and biological properties into the scaffold.

References

Dorozhkin S V 2007 *J. Mater. Sci.* **42** 1061
Mann S and Ozin G A 1996 *Nature* **382** 313
Nayar S and Sinha A 2004 *Colloid & Surface* **B35** 29
Sinha A, Das S K, Rao V and Ramachandrarao P 2001 *J. Mater. Res.* **46** 1846
Sinha A, Nayar S, Agrawal A, Bhattacharya D and Ramachandrarao P 2003 *J. Am. Ceram. Soc.* **86** 357
Sinha A, Nayar S, Agrawal A, Rao V and Ramachandra Rao P 2005 Indian Patent 'A process for preparation of nanosize hydroxyapatite by a biomimetic route', Patent Number 192392
Sinha A, Das G, Sharma B K, Roy R P, Pramanik A K and Nayar S 2007 *Mater. Sci. Engg.* **C27** 70

Freezing as a Path to Build Complex Composites
複雑な合成物を造るための経路としての凍結

Abstract

Materials that are strong, ultralightweight, and tough are in demand for a range of applications, requiring architectures and components carefully designed from the micrometer down to the nanometer scale. Nacre, a structure found in many molluscan shells, and bone are frequently used as examples for how nature achieves this through hybrid organic-inorganic composites. Unfortunately, it has proven extremely difficult to transcribe nacre-like clever designs into synthetic materials, partly because their intricate structures need to be replicated at several length scales. We demonstrate how the physics of ice formation can be used to develop sophisticated porous and layered-hybrid materials, including artificial bone, ceramic-metal composites, and porous scaffolds for osseous tissue regeneration with strengths up to four times higher than those of materials currently used for implantation

・序論

　層をなした材料は強度が強くて軽く応用の幅が広い。しかし、軟体動物の殻が持つような精巧な真珠層はマイクロメートルからナノメートルまで変化していて、合成物で再現することは非常に困難であった。そこで目を付けたのが海水であり、海水は氷結する際に層を形成し、不純物は結晶の層間に閉じ込められて真珠層のような構造をとることがわかった。

この自然の原理を利用してセラミックから二段階のアプローチ（初めに、セラミック懸濁液の凍結の方向性を制御しての凍結除去過程を経て、1μmほどの細い層を形成する。この多孔質の足場に有機または無機の相を満たし高密度の複合体を作る。）で簡単に真珠層を形成できるのではないかと考えた。

・本文

　層をなした材料の可能性は認められてきてるとはいえ、これらの創造物は微細構造の最適条件や、製作手順の開発を実行するために、これら2つの問題を解決する必要がある。真珠層のような天然材料はデザイン過程を導くための多くの情報を提供されている。自然に層をなした材料の特有の性質は、正しい成分の選択、そして、有機・無機界面でのラフネスと接着性の操作などの層の厚さの細かい操作によって成し遂げられる。理想の製作の過程は、簡単なだけでなく、材料の組み合わせで十分な層の厚さを造り、層の面積の幅広さを造る多くの順応性が必要である。真珠層を模造するための以前の技術では、厳密な界面

相互作用や互換性を示すことは本質的に材料の狭い範囲に限られている。他の技術では、層の厚さの細かいコントロールまたは、形成することのできる層の多くに関しては事実上限定である。

海水の氷では、C結晶軸が水平方向にランダム配向した純粋な六角形の板状結晶が形成された。そして、海水中に存在する独自の多様な不純物は、形成した氷から除去され、氷の結晶間の溝に閉じ込められる。我々は、水中にセラミックス粒子を散乱させ、二段階のアプローチで真珠層のような洗練させた構造を作るために自然の原理を利用した。氷鋳型、多孔質、層をなした材料はセラミック懸濁液の一方向の凍結の制御を含む凍結除去過程を通して、初めに $1\,\mu m$ 程度の細い層を形成する。これらの多孔質の足場は、高密度の複合体を形成するために、選択された第二の相 (有機または無機) に満たされる。

水の凍結の物理学は長年の間科学者を引き付けてきた。ほとんど例外がなく、この研究の多くは、純水の凍結や懸濁液の希釈に集中していた。この現象は生物細胞の懸濁液の低温保存や、汚染物質の浄化として重要な多種の応用であった。これらの研究の重要な観察は、懸濁液の凍結の間、移動する氷前線によって懸濁液粒子は閉じ込められ、重要な粒子サイズになることである。残りの重要な観察は、結晶方向を二桁以上に変えられ、六角形氷結晶は強い異方性を示す。このようにラメラ微細構造は形成され、厚さは主に凍結前線速度に依存する。濃縮された懸濁液の凍結によって、セラミック粒子は適合粒度分布を含んでいる。我々は均一に層をなした多孔質の足場を形成できるであろう。

ここに材料と方法を示した。セラミックスラリーの凍結方向は二つの銅の氷指紋の間に置いたポリテトラフルオロエチレンの型に流すことによって成し遂げられる。温度は凝固前線の速度を操作することで調節した。天然物として、海水が凍結してる間、セラミック粒子は氷結晶の間に濃縮される。凍結速度が増加すると、凝固界面の前に過冷却の大きさが増加する、そして、その結果して氷構造の先端半径は減少する。細かい微細構造は全体の長い幅での配列作用なしに得られる。その後、その氷は凍結乾燥で昇華させ、セラミックの足場での微細構造が氷の反対の方法で生み出された。我々は凍結動力学の適合によってラメラの成長を制御した。この方法で、我々は $1\,\mu m \sim 200\,\mu m$ で二桁以上変化できる適切な次元をもつ微細構造を成し遂げた。大部分は、これらの機械的な応答は天然材料の中間構造が決定する、そして、この中間構造は自己複製が困難である。我々の結果を示す、氷指紋の凍結動力学とデザインをコントロールすることで、中間構造の特徴と勾配を構築することを可能にし、最終的な材料の機械的応答を最適化することができた、例えば、構造の堅さや、ねじりの限界などである。

氷鋳型の多孔質の足場は、真珠層の無機構成成分の中間構造や微細構造と強い類似性を示すこの方法によって得られる。無機層は全体の試料を通して均一にそして、お互いに水

平方向に配列している。粒子は真珠層のように壁の樹枝状の表面の粗さを導くために、氷樹状突起の間に閉じ込められる。最終的に、いくつかの樹状突起はラメラ間の溝を補い、転写することは、小さな無機層の橋と真珠層の無機層プレートを連結することで、破砕抵抗が増加するであろう。

真珠層の容量の 95 % に相当する無機層の一部の特有の性質は、有機相と炭酸カルシウムプレートの間に見つかった層の構成要素の相が作用によるものである。類似した合成材料を得るために、我々は次に第二の相に多孔質足場を満たした。例えば、氷鋳型の足場をシンプルな有機相へ、または、無機構成成分へ満たした。天然物は破砕特性が有機無機界面で強いだけでなく、有機無機界面で起こる層間剥離に出くわすことで起こると示している。氷鋳型では層間での広い亀裂の片寄が観察された。天然物のように、この層間剥離が創る捻れた亀裂は材料の堅さを増加させる。自然が操作する接着を機械的と化学的の二つの方法で操作できると信じている。真珠層では、粗さの制御、そして、重合接着層の高度な特異性質によって行える。我々の過程は無機層の形態学、そして、界面の化学を制御することで可能にする。例えば、アルミナの層をなした複合体の機械的性質は界面の結合の制御によって操作することができる。0.5 % と少量のチタンを加えることで、アルミナとの共晶は強度が 400 から 600 MPa に増加し、破壊靭性が 5.5 から 10 MPa / m$^{1/2}$ に増加した。

我々の技術のサイズの合う複合材料のを必要とする多くの応用のための裏付けを示している。このような科学的試みは、設計分野のための新しいバイオ材料の開発をすることができる。骨の再生のための多孔質の足場の開発は広い展開にもかかわらず、全ての材料の持つ本来の強度の欠乏は間隙率と結びつける。市販アパタイトの懸濁液を凍結して利用することによって、圧縮試験で通常の多孔質 HAp と比べ 4 倍強い氷鋳型の多孔質の足場が得られた。これらの氷鋳型の足場は骨内成長を可能にする適切の大きさの間隙率と方向性を、十分明確に示している。今後、病い骨変換のための現在の欠点はこ革新的なアプローチで除去される。

現在のセラミックや金属インプラントは骨との物理的性質のミスマッチのために深刻な欠点を持つ。骨の中で、リン酸カルシウムやコラーゲンのように中間体率を示す複合物の中で接着している本質的に弱い材料は高度な強度、高度な破砕力を示している。骨の特有の性質は有機物の結合の制御やナノから中間レベルからの無機構成要素の洗練された構造から生まれる。この問題に対する我々のアプローチは調整された生物分解性を持つ第二の有機相へ氷鋳型の多孔質の足場を浸透させること。なぜなら、足場の生物分解性や浸透させた合成物は異なるデザインをでき、多孔性はインサイチューでの骨の成長を可能にする。このアプローチを用いることで、剛性率 10 MPa, 強度 150 MPa, 破砕力 220 J / m^2, ミネラルと有機物 60 / 40 vol % の緻密な骨とマッチする HAp と塩基の複合体を造ることができるだ

ろう。

文献紹介

Biomimetic synthesis of hybrid nanocomposite scaffolds by freeze-thawing and freeze-drying
凍結解凍と凍結乾燥でのハイブリッドナノ複合体足場の生体模倣合成

・序論

ナノ粒子の合成でもっとも重要な論点の一つとして粒子サイズと形状の調整の仕方が知られている。生体模倣は母体とデザインの実行とナノスケール材料の合成から構想を得て、機能的なナノ材料と構造を創り出すことに成功している。生体を模倣した合成はインサイチューでの核形成と前組織化された有機鋳型中での無機ナノ粒子の成長を実現する。界面での相互作用によって純粋な高分子—無機混合物の機能性質より良く、親水性高分子は前組織化された鋳型として組織工学のための高分子-無機ナノ複合体を含めるナノシステムの広い範囲の生体模倣の合成に用いられている。親水性高分子のポリビニルアルコール（PVA）中での Hap の合成は、本来の Hap が持つ乏しい機械的性質を補い、骨と軟骨のつなぎとしての足場の異なる形状を創りだす可能性を持っていた。この研究では、PVA 中での Hap の合成を、凍結乾燥を用いる事で 2 次元の平面板に、凍結解凍を用いる事で 3 次元の塊を形成させ、X 線回折、走査型電子顕微鏡観察、原子間力顕微鏡観察により両形状の特徴を調べた。

・本文

　ナノ粒子の一つの重要な論点として、粒子サイズや形態の調整の仕方が知られている。生体模倣、母体やデザインの実行やナノスケール材料の合成から構想を得て、機能的なナノ材料や構造を創り出すことに成功した。生体模倣合成はインサイチューでの核形成や組織化された有機鋳型中での無機ナノ粒子の成長を実現する。洗練された微細構造は無機 -高分子混合物よりよい機能性質を供給する界面の相互作用によって成し遂げられる。これは異なる親水性高分子は組織工学のための高分子 - 無機複合体を含めるナノシステムの広い範囲の生体模倣合成中の前組織化された鋳型として用いることができると確立した。そこで、我々はポリビニルアルコール用いた。人工骨の主要成分に非常に類似した化学合成物のために、HAp で強化された高分子ナノ複合体は医療分野の移植組織に徐々に用いられるようになった。PVA 中での HAp のインサイチューの合成は、HAp の乏しい機械的性質を克服するだけでなく、骨や軟骨をつなぐための混成の足場の異なる形状を生み出すための広い可能性を供給した。これらの混成材料の分子認識は形状制御や HAp ナノ粒子の次元だけでなく、より高い次元にこれらを集める。この研究では、どのように当初の PVA 中での HAp の生体模倣合成がことなるか、二つの異なる合成過程技術が二つの異なる足場の形

成を導くか述べる。凍結乾燥後の二次元の平面板、凍結解凍のサイクルが実現した三次元の塊は形成される。どちらの足場も X 線回折、走査型電子顕微鏡観察、原子力顕微鏡観察で特徴づけた。

PVA 中での HAp の生体模倣合成は我々の研究所で確立された、そして、我々のグループによって過程を始めた。二次元の構造、三次元の塊を得る目的で、この過程を低い温度に調整し、凍結乾燥と凍結解凍によって成し遂げた。凍結乾燥は−80 ℃ に温度を急激に落としたのに対し、凍結解凍は乾燥と解凍を繰り返し循環させた、その点で水はシステム中に閉じ込められ保持された。凍結乾燥する間、最終的なスラリーは−80 ℃ で 36-48 時間 0.03 ミリバールの非常に細かい吸引で乾燥され、包んで、4 ℃ に保たれた凍結冷蔵庫で凍結解凍した。それは凍結させてその後室温で解凍した。この温度の循環は平均約 15 回繰り返され、それによって良いヒドロゲルが得られた。

骨はセラミックタブレットと有機接合剤から形成された階層組織ナノ複合体であり、それによって材料科学者に広大な関心を与えた。PVA は親水性ポリマーとして知られていて、我々はこの能力をインサイチューでの HAp の核形成の触媒に利用した、しかしながら、高分子鋳型中での鈍い拡散過程により成長は限界に留まる。塊は X 線回折で水分子を閉じ込めてしまうために結晶性がほとんどないと示している。走査型電子顕微鏡観察では両足場は直径 100-150 nm の幅を持つ架橋された PVA-HAp ナノ繊維の不織布の構造が作られていた。試料の透過型電子顕微鏡解析は PVA ナノ混成物は HAp ナノ粒子で高度な無機物化を確認した。板状のようなナノ複合体は約〜10 nm の HAp 粒子を示した。しかしながら、相対的に塊は PVA-HAp 中で大きな粒子サイズが得られた。

粒子先端の相互作用の形態画像を示す。透過型電子顕微鏡のデータに従って、原子間力顕微鏡は明白な密集または、凍結乾燥した試料と比較して凍結解凍した試料の方が成長しているのを示している。どちらも合成 HAp 粒子の狭い大きさでの配置効果がある。
足場は組織工学の模造の細胞外マトリックスに用いられ、細胞接着、移動、移植を支える。

結果をここに示し、生来の高分子化学でナノテクノロジーに貢献する共生の関係の優秀な実例を提供する。我々は HAp、PVA、コラーゲンを用いた板状、塊状の足場の合成を始め、結果促進した。重合によるシステムでは、ナノ構造は反応器なしでのナノ粒子の成長の役割を果たしている。これらの材料は簡単なだけでなく、安価である。これらは粒子の成長の制御も行う。我々の結果が微細構造や機械的性質の向上を示しているのにかかわらず、理想の組織工学のためには望まれる組織は足場中で化学工学的、機械的、生物学性質に原型として用いられるべきである。

文献紹介

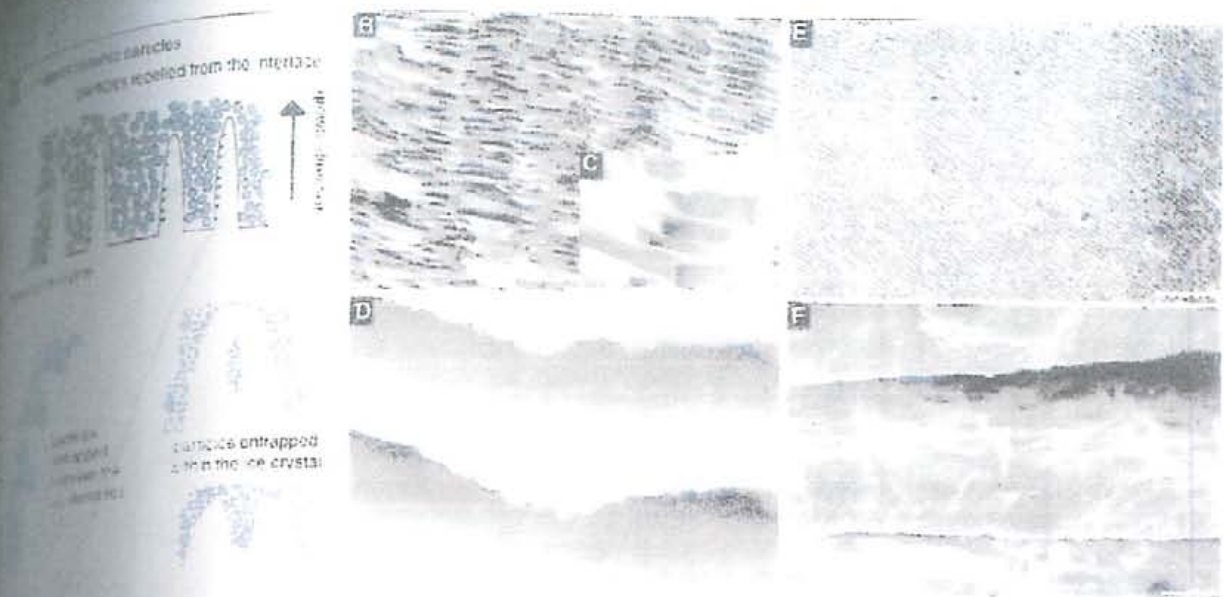# Freezing as a Path to Build Complex Composites
## 複雑な合成物を造るための経路としての凍結

Abstract

Materials that are strong, ultralightweight, and tough are in demand for a range of applications, requiring architectures and components carefully designed from the micrometer down to the nanometer scale. Nacre, a structure found in many molluscan shells, and bone are frequently used as examples for how nature achieves this through hybrid organic-inorganic composites. Unfortunately, it has proven extremely difficult to transcribe nacre-like clever designs into synthetic materials, partly because their intricate structures need to be replicated at several length scales. We demonstrate how the physics of ice formation can be used to develop sophisticated porous and layered-hybrid materials, including artificial bone, ceramic-metal composites, and porous scaffolds for osseous tissue regeneration with strengths up to four times higher than those of materials currently used for implantation

・序論

層をなした材料は強度が強くて軽く応用の幅が広い。しかし、軟体動物の殻が持つような精巧な真珠層はマイクロメートルからナノメートルまで変化していて、合成物で再現することは非常に困難であった。そこで目を付けたのが海水であり、海水は氷結する際に層を形成し、不純物は結晶の層間に閉じ込められて真珠層のような構造をとることがわかった。この自然の原理を利用してセラミックから二段階のアプローチ（初めに、セラミック懸濁液の凍結の方向性を制御しての凍結除去過程を経て、1μm ほどの細い層を形成する。この多孔質の足場に有機または無機の相を満たし高密度の複合体を作る。）で簡単に真珠層を形成できるのではないかと考えた。
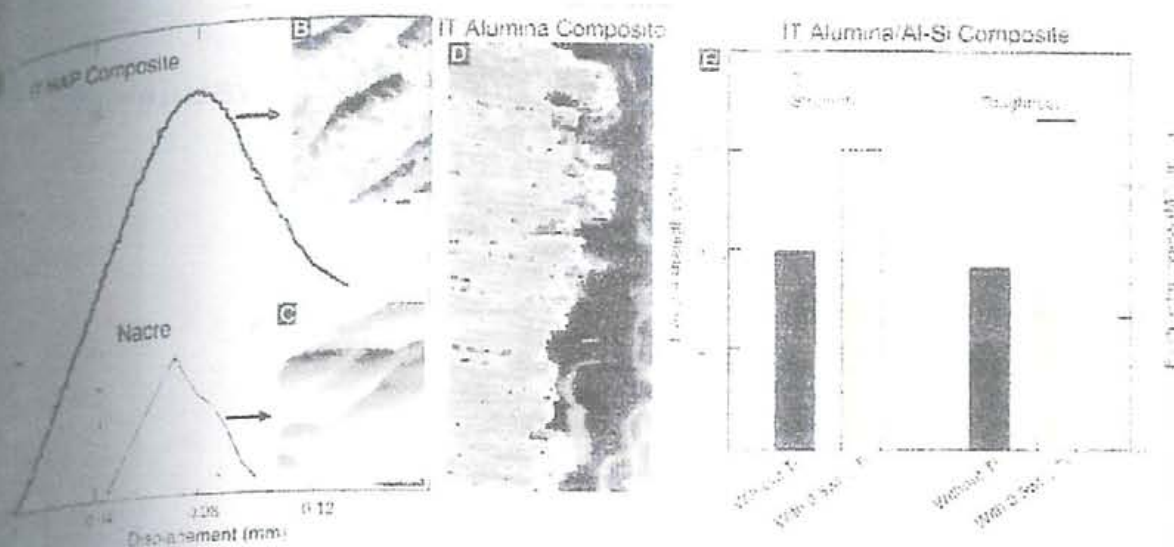
セラミック懸濁液を型に流し込み凍結の方向を決め、凍結速度の調整を行い、氷を昇華させて取り除くと、セラミック懸濁液は、氷結晶の成長によりセラミック粒子を排出し、氷結晶の動きに平行な方向にラメラ構造をつくりだす。高度に濃縮されたセラミック懸濁液の粒子は小さくなり、先端分離によって氷結晶に閉じ込められ、再生し隣接した壁間に無機の橋を形成した。ことの小さな無機層の橋真珠層の無機層プレートの連結により破壊抵抗が増すと考えられている。
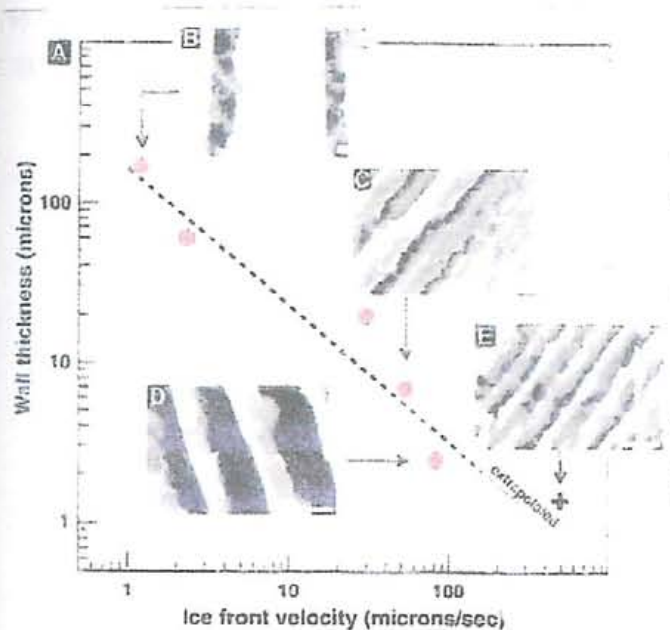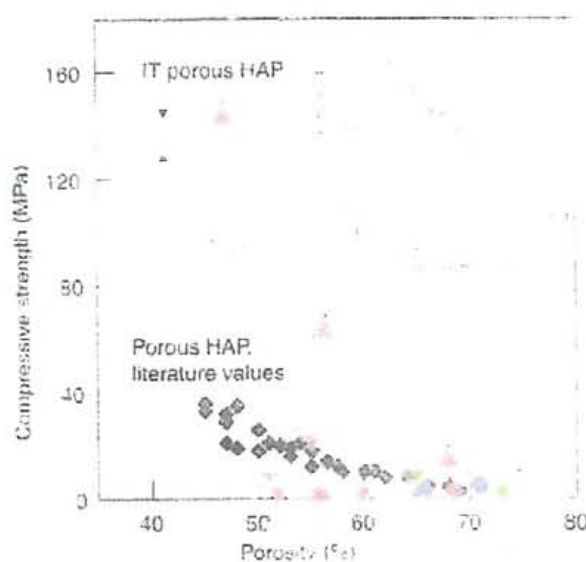

凍結速度を変えることによって、層状構造のサイズが小さくなることがわかった。この技術での壁厚の限界を調べた(E)では 1 μm であり、一般的な真珠層の 0.5 μm に近い微細構造が得られた。

凍結動力学と氷指紋のデザインの制御によって真珠層の無機構成要素の中間構造や微細構造と強い類似性を示す氷鋳型の多孔質の足場が得られた。

IT HAP Composite / B / IT Alumina Composite / D / IT Alumina/Al-Si Composite / E / Nacre / Displacement (mm)

割れた氷鋳型の足場にエポキシまたは金属で満たすと、(B), (D)の氷鋳型の複合体では層
間の界面での広い亀裂が観察され、(C)の真珠層ではこの層間剥離が創り出すねじれた亀裂
が材料の靭性を増加させていた。真珠層に習った無機層の形態学と界面化学の制御によっ
て強度を増すことができると考え、Al-Si (45/55 vol %)に 0.5 wt % と少量の Ti を加えて界
面の結合の制御を行なったところ、強度が 400 から 600 MPa に、破壊靭性が 5.5 から 10
MPa / m^{1} に増加した。

IT porous HAP / Compressive strength (MPa) / Porous HAP, literature values / Porosity (%)

Hap 粉末の懸濁液を処理して高度な氷鋳型のラメラ多孔質の足場を形成したものは圧
縮試験で通常の多孔質 Hap の 4 倍高い値を示した。
現在人工骨として使用されているセラミックや金属インプラントは物理的性質で合わない。
しかし、氷鋳型の多孔質 Hap に分解性のある有機相を浸透させ、体内で骨成長を促進する

成分を放出できれば古い骨と新しい骨の融合ができると考えられ、現在も研究が進められています。

Biomimetic synthesis of hybrid nanocomposite scaffolds by freeze-thawing and freeze-drying
凍結解凍と凍結乾燥でのハイブリッドナノ複合体足場の生体模倣合成

Abstract. The aim of this study is to biomimetically synthesize hydroxyapatite–hydrophilic polymer scaffolds for biomedical applications. This organic–inorganic hybrid has been structurally characterized and reveals a good microstructural control as seen by the SEM analysis and the nanosize of the particulates is confirmed by AFM microscopy. The characterization of such nano-structured composites would allow researchers to design new systems, tailoring properties for different applications.

・序論

ナノ粒子の合成でもっとも重要な論点の一つとして粒子サイズと形状の調整の仕方が知られている。生体模倣は母体とデザインの実行とナノスケール材料の合成から構想を得て、機能的なナノ材料と構造を創り出すことに成功している。生体を模倣した合成はインサイテューでの核形成と前組織化された有機鋳型中での無機ナノ粒子の成長を実現する。界面での相互作用によって純粋な高分子―無機混合物の機能性質より良く、親水性高分子は前組織化された鋳型として組織工学のための高分子-無機ナノ複合体を含めるナノシステムの広い範囲の生体模倣の合成に用いられている。親水性高分子のポリビニルアルコール（PVA）中での Hap の合成は、本来の Hap が持つ乏しい機械的性質を補い、骨と軟骨のつなぎとしての足場の異なる形状を創りだす可能性を持っていた。この研究では、PVA 中での Hap の合成を、凍結乾燥を用いる事で 2 次元の平面板に、凍結解凍を用いる事で 3 次元の塊を形成させ、X 線回折、走査型電子顕微鏡観察、原子間力顕微鏡観察により両形状の特徴を調べた。

・実験

凍結乾燥は温度を約−80℃まで急激に下げたのに対し、凍結解凍は凍結と解凍を繰り返し循環させることで水を組織内に閉じ込めて保持した。最終的なスラリーは−80℃、0.03 ミリバールの細かい吸引で 36-48 時間乾燥し、4℃に保たれた凍結が自由に行える冷蔵庫内に包んで入れた。この冷蔵庫を用いて凍結と室温での解凍を平均 15 回行った。
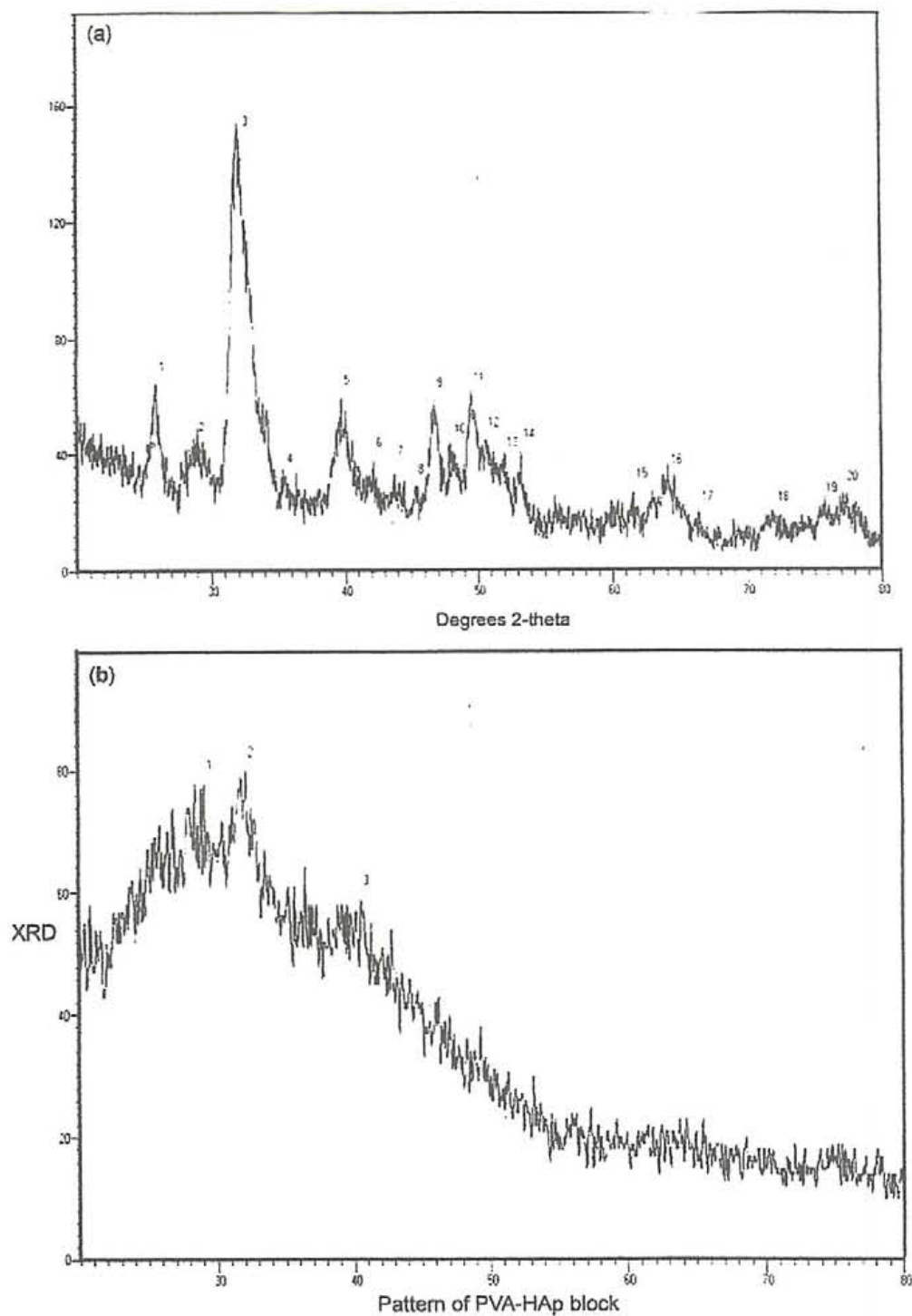
Figure 1. XRD patterns of (a) PVA–HAp sheet and (b) PVA–HAp block.

X線回折結果では板状は(2 1 0),(1 1 2),(3 1 0),(2 2 1),(1 1 3)、塊状は(2 1 0),(1 1 2),(2 2 1)にHapの特徴的なピークを示した。結晶性の評価は核形成のための触媒である有機表面のエネルギーに帰するが、塊状のX線回折結果では水分子を閉じ込めてしまうために結晶性がほとんど見られない。
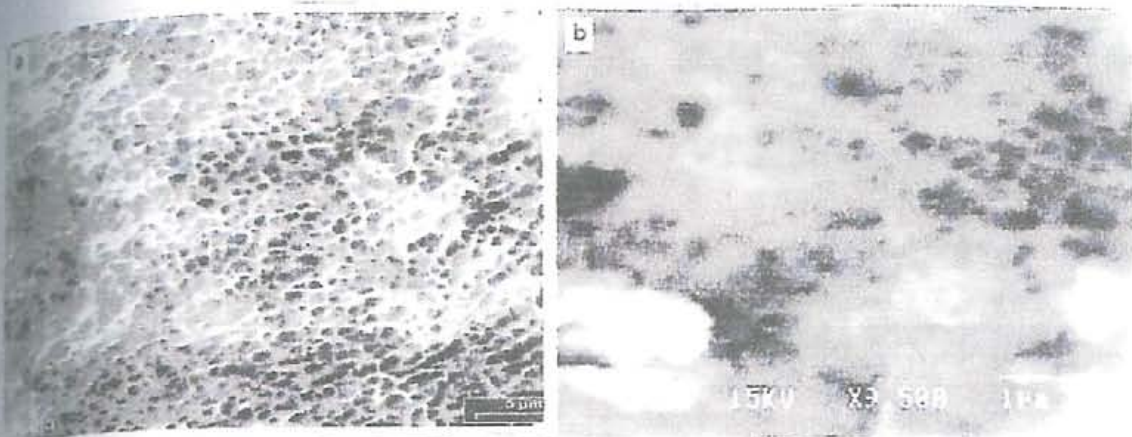
Figure 2. SEM micrographs of a. PVA-HAp nanocomposite sheet and b. PVA-HAp nanocomposite block.

SEM 画像では両足場は直径 100-150nm の PVA-Hap ナノ繊維が架橋となった不織布の構造が作られていた。

TEM での解析で板状が粒子サイズ 10nm までなのに対し、塊状は 80-100nm であった。この理由としては、PVA 中での Hap 粒子が成長するのに十分な拡散時間を与えた事によるものと考えられている。
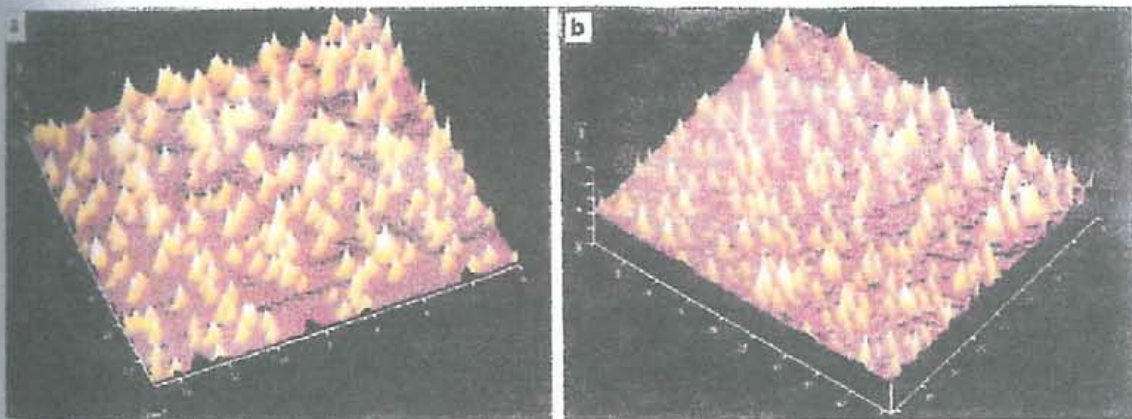

Figure 4. AFM topography revealing nanosized HAp particles in a. PVA sheet and b. PVA block.

AFM画像では凍結乾燥した試料と比較すると凍結解凍した試料の方が明かに密集または成長していて、合成 Hap 粒子は狭く配置されている。

足場は組織工学で天然の細胞外マトックリクスの模造に用いられ、細胞の粘着、移動、増殖を支えている。